JOURNAL OF GEOPHYSICAL RESEARCH, VOL. 114, B04409, doi:10.1029/2008JB005683, 2009

Constitutive properties of clayey fault gouge from the Hanaore fault zone, southwest Japan

Hiroyuki Noda[1,2] and Toshihiko Shimamoto[3]

Received 11 March 2008; revised 15 August 2008; accepted 11 February 2009; published 22 April 2009.

[1] Velocity step tests at a range of slip rates (0.0154–155.54 μm s^{-1}) are performed using natural fault gouge containing smectite, mica, and quartz collected from an outcrop of the Hanaore Fault, southwest Japan. Field and microscopic observations reveal that the shear deformation is localized to a few centimeters or thinner layer of black clayey fault gouge. This layer is formed by multiple stages, and determining the width of the shear zone due to a single event is difficult to determine. The experimental data on the abrupt jumps in the load point velocity are fitted by a rate- and state-dependent frictional law, coupled with the spring-slider model, the stiffness of which is treated as a fitting parameter. This treatment is shown to be essential to determine the constitutive parameters and their errors. The velocity steps are successfully fit with typically two state variables: larger b_1 with shorter d_{c1} and smaller b_2 with longer d_{c2}. At slip rates higher than 1 μm s^{-1}, negative b_2 is required to fit the data in most of the cases. Thin gouge layers ($\sim$200 μm) in the experiment enables us to simulate large averaged shear strain which is important to recognize the evolution of the state variable associated with negative b_2 and long d_{c2}. Observation of microscopic structure after experiments shows poor development of Y planes. This may be consistent with the mechanical behavior observed: weak occurrence of initial peak strength at yielding and displacement hardening throughout the experiments.

Citation: Noda, H., and T. Shimamoto (2009), Constitutive properties of clayey fault gouge from the Hanaore fault zone, southwest Japan, *J. Geophys. Res.*, *114*, B04409, doi:10.1029/2008JB005683.

1. Introduction

[2] An earthquake cycle involves very wide slip rates ranging from ultraslow rates much lower than plate velocity ($<10^{-9}$ m s^{-1}) to high rates during seismic fault motion ($\sim$1–10 m s^{-1}). Thus, modeling of an earthquake cycle requires fault constitutive laws over such wide slip rates. Understanding the frictional behaviors of faults was improved by rate- and state-dependent frictional laws [*Dieterich*, 1979; *Ruina*, 1983] at slip rates around 1 μm s^{-1}, which has been successfully used in the analyses of earthquake nucleation, rupture propagation and earthquake cycles [e.g., *Tse and Rice*, 1986; *Lapusta et al.*, 2000; *Lapusta and Rice*, 2003; *Hori et al.*, 2004; *Shibazaki et al.*, 2004]. Recent studies on high-velocity friction have revealed that frictional properties change dramatically owing to frictional heating at high slip rates and large displacements; i.e., effect of frictional melting [*Tsutsumi and Shimamoto*, 1997; *Hirose and Shimamoto*, 2005; *Di Toro et al.*, 2006; *Sirono et al.*, 2006; *Nielsen et al.*, 2008], thermal pressurization [*Sibson*, 1973; *Lachenbruch*, 1980; *Mase and Smith*, 1985, 1987; *Andrews*, 2002; *Wibberley and Shimamoto*, 2005; *Noda and Shimamoto*, 2005; *Bizzarri and Cocco*, 2006a, 2006b; *Rice*, 2006], and high-velocity friction of faults with or without gouge [*Tsutsumi and Shimamoto*, 1997; *Tullis and Goldsby*, 2003; *Di Toro et al.*, 2004; *Mizoguchi et al.*, 2007; *Han et al.*, 2007; *Hirose and Bystricky*, 2007]. How the conventional rate- and state-dependent laws change for friction at high-velocity still remains to be explored.

[3] We have been studying the frictional properties of the Hanaore fault in an attempt to establish fault constitutive laws from slow to high slip rates. The Hanaore fault is one of the major active faults in Japan, developed in Jurassic accretionary complex in Kyoto Prefecture [e.g., *Yoshioka et al.*, 2000]. We have already reported an analysis of thermal pressurization processes at seismic slip rates based on measured transport properties of this fault zone [*Noda and Shimamoto*, 2005]. This paper reports complex constitutive properties of the Hanaore fault zones at slow slip rates based on velocity step experiments and a new inversion method of estimating constitutive parameters, using a high-temperature biaxial frictional testing machine [*Kawamoto and Shimamoto*, 1997, 1998]. The frictional behavior of Hanaore fault gauge at high and intermediate slip rates will be reported elsewhere. We hope that this series of studies will elucidate frictional properties of the Hanaore fault over a wide range of slip rates. This can be used for the modeling of complete earthquake

[1]Department of Geophysics, Division of Earth and Planetary Sciences, Graduate School of Science, Kyoto University, Kyoto, Japan.
[2]Now at Seismological Laboratory, California Institute of Technology, Pasadena, California, USA.
[3]Department of Earth and Planetary Systems Science, Graduate School of Science, Hiroshima University, Higashi-Hiroshima, Japan.

0148-0227/09/2008JB005683$09.00

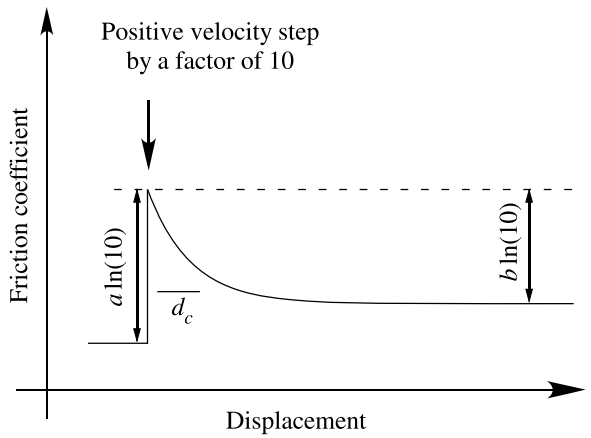

Figure 1. A schematic diagram of mechanical behavior of a simulated fault obeying rate- and state-dependent frictional law with abrupt change in slip rate.

cycles. Most active faults in Japan are typically developed either within accretionary complexes (metamorphosed or nonmetamorphosed) or in granitic basement rocks. Fault gouge from an outcrop of the Hanaore fault zone probably represents shallow fault zones developed in an accretionary complex, comprising mostly sandstones, shale, siltstones and some volcanics.

[4] We have used a biaxial frictional testing machine to enable experimental determination of the constitutive parameters of the Hanaore fault gouge because its loading system is free from O-ring friction and jacket strength, and consequently very sensitive measurements of friction is possible. We attempt to increase the accuracy of the estimate of the parameters along two lines: (1) eliminating the unpredictable error caused by the fluctuating machine stiffness by treating the stiffness as an unknown in the analysis of fault-machine interaction to obtain the constitutive parameters and (2) attaining as much shear strain as possible to determine full sets of two-state variable constitutive parameters within the limit of total displacement (20 mm in our case). Our intent for each is now discussed.

[5] In many testing machines, a step change in velocity is assigned at a load point. We impose a step change by changing the motor speed and/or by changing the gear assembly instantly by using electromagnetic clutches, without stopping the motor of the testing machine. In such cases the machine always interacts with fault motion, causing a certain amount of slip toward the peak friction due to the direct effect followed by transient change in friction toward the steady state. But the value of the machine stiffness has some uncertainty as shown in stick-slip experiments (e.g., *Shimamoto et al.* [1980] and *Ohnaka* [1973] or as reported by *Blanpied et al.* [1998]). In this work we investigate the mechanical response of the apparatus to loading, show under what condition this uncertainty is critical, and propose a new inversion method with which we can determine the set of fault constitutive parameters and their errors. However, this effect may not be so important in some circumstances; for example, the stiffness of the apparatus is determined accurately enough by the high-speed servo-control, or that the amplitude of the noise in the recorded data is large.

[6] The second problem is how to recognize steady state after a step change in slip rate. For example, *Blanpied et al.* [1998] show that experimental data are better fit with two state variables for granite at high temperature with pore water: positive b_1 with short d_{c1} and negative b_2 with long d_{c2}. Such a set of constitutive parameters predict a mechanical behavior in which the peak due to the direct effect on a velocity step is followed by a short decay and then by another long decay in the opposite direction. The first decay appears like a complete behavior upon a step change in slip rate in real experiments, but longer displacements are needed to determine full sets of constitutive parameters. This is a very difficult problem since one can point out a possibility of having a very large d_c to argue for deficiency of experiments. Only high-quality torsion machines with unlimited displacement can examine this problem (serpentine gouge [*Reinen et al.*, 1994]), and our biaxial machine suffers from limited displacement. However, we have tried to improve our measurements by using gouge as thin as 200 μm (about 10 times as thin as that used, e.g., by *Mair and Marone* [1999] and *Saffer and Marone* [2003]), allowing the average shear strain (displacement divided by gouge thickness) of near 100. In this way, the aim is to study a large-strain behavior in our experiments. Microstructures of the experimentally deformed gouge are compared with natural samples collected from the Hanaore fault zones to discuss how much natural deformation we have reproduced.

[7] Rate- and state-dependent frictional constitutive laws proposed by *Dieterich* [1979] and *Ruina* [1983] can describe the response of a sliding surface upon a step change in slip rate; that is, the amount of instantaneous response is characterized by a constitutive parameter a, and friction coefficient evolves in a transient manner by the amount characterized by b over a critical displacement d_c toward the steady state (e.g., a case for step increase in slip rate in Figure 1). The slip rate dependence of the steady state friction is given by $(a-b)$; positive for velocity strengthening and negative for velocity weakening. Despite great successes of the constitutive laws, real fault behaviors are much more complex than those described by the law with fixed constitutive parameters. For instance, experimental results by *Saffer and Marone* [2003] showed that the constitutive parameters for artificially mixed smectite-quartz gouge dramatically changes with conditions (i.e., $(a-b)$ changes from negative to positive at a slip rate of around tens of microns per second). In this paper, we report the determined frictional constitutive parameters of natural fault gouge for a wide range of slip rates from 0.0154 to 155.54 μm s^{-1}.

2. Internal Structure of the Hanaore Fault Zone at Tochudani Outcrop

[8] The Hanaore Fault is one of the major active faults in southwest Japan and is developed in pelitic rocks within the Mino-Tamba belt (Jurassic accretionary complex) and Cretaceous granitic rocks. The fault extends in a NNE–SSW direction from position (135°47′E, 35°1′N) to (135°56′E, 35°25′N) for about 50 km [*Research Group for Active Faults of Japan*, 1992; *Yoshioka et al.*, 2000] (Figure 2a). Dragging of strata around the Hanaore fault indicates left-lateral motion, but its predominant motion in the Quaternary

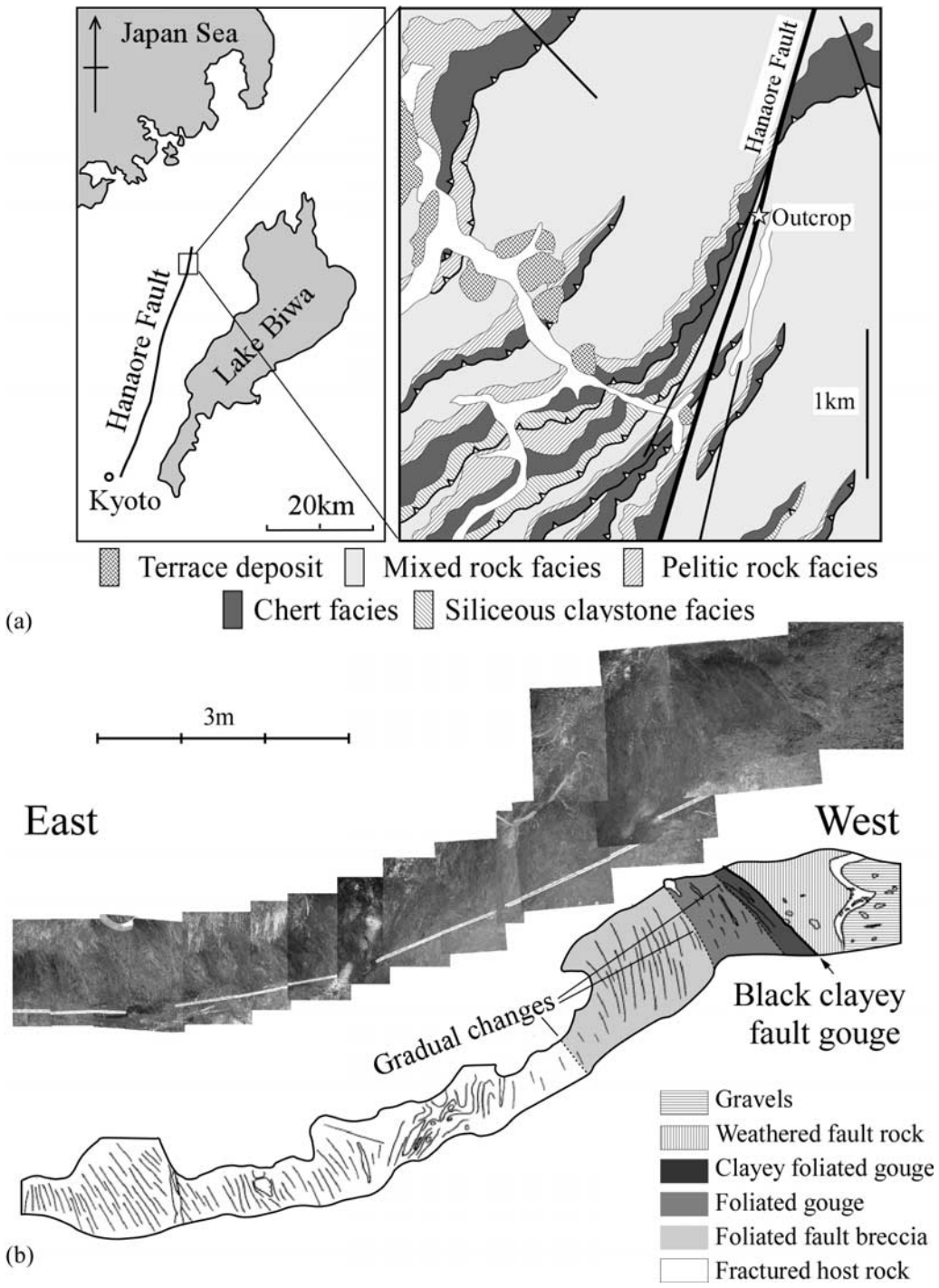

Figure 2. (a) Geological map around the outcrop studied. (b) (top) A photograph and (bottom) sketch of the outcrop.

is right-lateral strike slip. Trench excavations done in the northernmost portion of the Hanaore fault in the Tochudani area revealed that several meters of displacement had taken place during the last event between 460 ± 60 ^{14}C years B.P. and 360 ± 60 ^{14}C years B.P., which may correspond to the disastrous Kambun earthquake in 1662 [*Togo et al.*, 1997; *Yoshioka et al.*, 1998].

[9] The fault outcrop studied is located along a small mountain valley in the Tochudani area, Imazu-cho, Takashima-gun, Shiga Prefecture (locality 1 of *Yoshioka et al.* [2000]; 135°55′56″E, 35°24′5″N). The host rock comprises mixed rock facies in the Mukugawa complex, which is one of the sedimentary complexes in the Tamba belt. It has sandstone and chert blocks embedded in black to dark gray poorly sorted mudstone matrix with strong cleavage [*Nakae and Yoshioka*, 1998].

[10] In this outcrop the fault zone consists of, from east to west (from left to right in Figure 2b), (1) ∼15 m wide

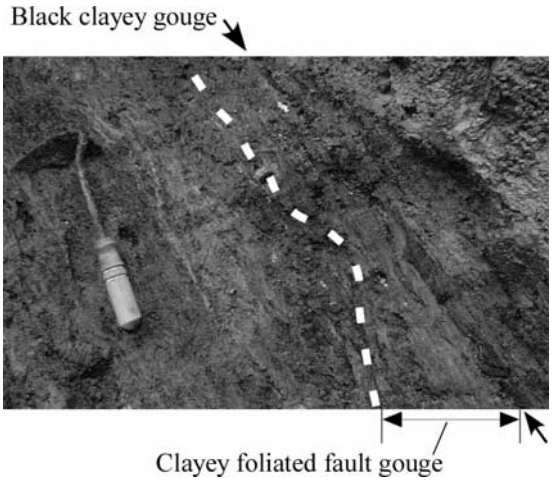

Figure 3. A photograph of the fault core where samples are collected.

fractured pelitic host rock, (2) ~5 m wide foliated fault breccia, (3) ~1 m wide foliated gouge, (4) ~100 mm wide clayey foliated fault gouge, (5) several to about 30 mm thick black clayey fault gouge, and (6) light brown weathered fault rock of several meters in width (Figure 2b). The changes between zones 1 and 4 are gradual and it is difficult to define clear boundaries between them, but there is clear discontinuity in color between zones 4 and 5 and between zones 5 and 6 (Figure 3). The westward extent of the fault zone is unclear.

[11] The mudstone matrix of zone 1 has strong cleavage (Figure 4a) and sometimes contains calcite veins or radiolaria fossils (Figure 4b). Within zone 2, fractures which are not parallel to the cleavage and weaker preferred orientation of platy minerals than observed in host rock, suggesting brecciation and rotation of fragments (Figure 4c). Zone 3 contains rounded clasts derived form sandstone, chert, and quarts vein (Figure 4d). Very fine grained thin black layers of less than 1 mm in width are observed under optical microscope (Figure 4e). They are observed also in zone 4. The foliation is developed primarily owing to preferred orientation of platy minerals as is typical of foliated fault gouge [*Chester et al.*, 1985]. Some deformation due to fault motion is likely to have concentrated on zone 4 with its foliation nearly parallel to zone 5 (see foliation from upper left to lower right in Figure 3). Figure 4f shows the contact of clayey foliated fault gouge and black clayey fault gouge. Although the width varies, zone 5 is developed straight and continuously separating zone s 4 and 6 (see an example between two arrows in Figure 3). The orientation of this slip zone (strike and dip in N30°E and 40°NW) is somewhat

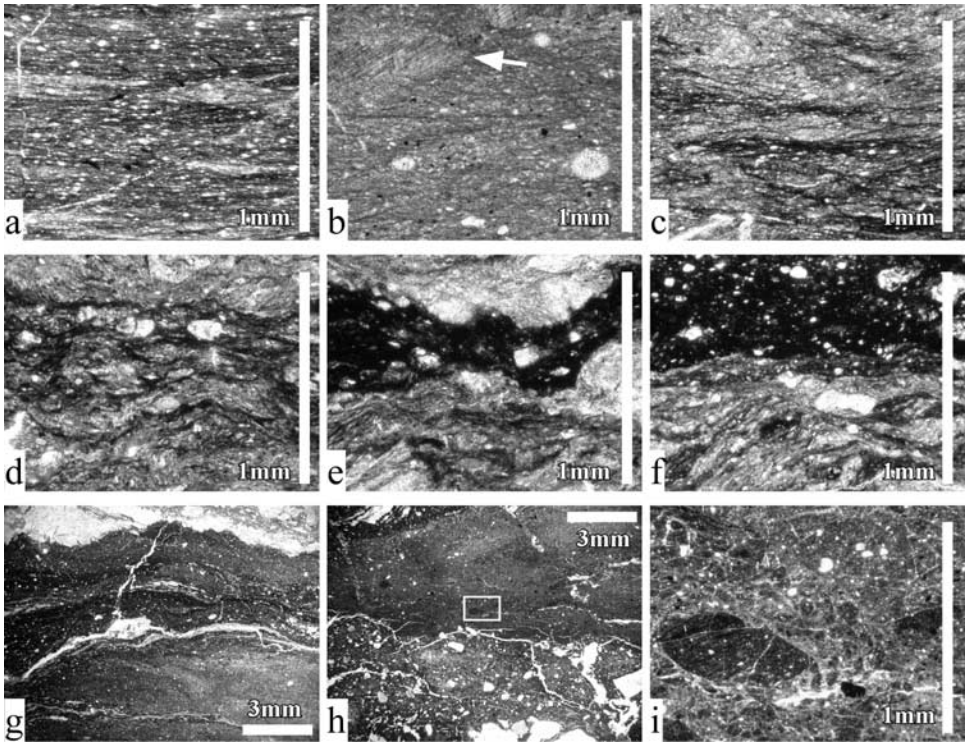

Figure 4. Microphotographs of thin sections. (a) Fine-grained black portion in fractured host rock. Cleavage is horizontal in the picture. (b) Coarse-grained gray portion in fractured host rock which contains Radiolaria fossils. There is a healed crack cemented by calcite (at the arrow). (c) Foliated fault breccia. The foliation is not from large deformation but from original foliation of host rock. (d) Foliated fault gouge. The foliation here is due to deformation. (e) Thin fine-grained black layer found in foliated fault gouge. (f) The very contact of clayey foliated fault gouge and black clayey fault gouge. (g) Strongly foliated portion in black clayey fault gouge. (h) Relatively random fabric portion in black clayey fault gouge. Lower portion of the picture contains many clusts. (i) The magnified picture indicated by white box in Figure 4h. Black clayey fault gouge contains clusts with gouge texture, which implies that multiple events took place here.

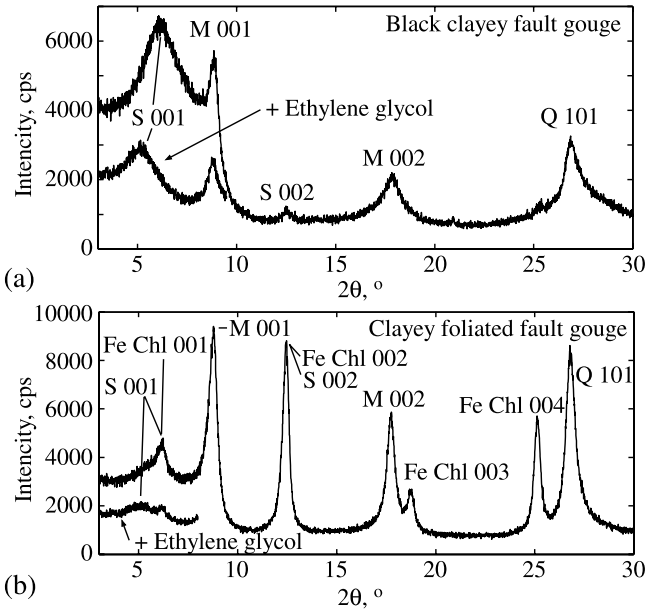

Figure 5. XRD analyses of (a) black clayey fault gouge and (b) clayey foliated fault gouge. Symbols attached to the peaks represents Q, quartz; M, mica; S, smectite; Fe Chl, Fe chlorite.

different from that of the Hanaore fault in this region (strike in N15°–23°E [*Yoshioka et al.*, 2000] and strike slip), so the slip zone may have rotated because of the latest fault motion. Zone 5 is more comminuted and indurated than zone 4 and has a variety of microstructures within its width, varying in fabric and the amount of clasts. Figure 4g shows a foliated portion, the thickness of which is several millimeters. Lower half of Figure 4h contains many large clasts consisting of quartz. Upper half of Figure 4h has black clasts with gouge fabric in it (Figure 4i), indicating that this portion experienced brittle deformation at least twice. The thickness of zone 5 does not directly reflect the thickness of a shear zone during a fault motion, and as such we do not know whether it was seismic or aseismic, but at least gives an upper limit to the instantaneous width of the shear strain distribution. The estimation of the width of shear zone of a slip event is very difficult solely based on microscopic observations. As shown in Figures 4g and 4h, zone 5 consists of layers of different textures which are around 5 mm in thickness. They are defined by clear boundaries along which there is no evidence of shear localization, such as preferred orientation of platy minerals. The microstructure of the clayey fault gouge at this outcrop is much more complicated than that reported in Punch Bowl Fault in California [*Chester et al.*, 2003; *Rice*, 2006] (a well-developed Y plane of hundreds of microns in thickness). XRD analyses of the oriented samples reveal that zone 4 contains Fe-chrolite, smectite, mica, and quartz (Figure 5b), and zone 5 contains smectite, mica, and quartz (Figure 5a).

3. Experimental Methodology

[12] The sample used in this work was collected from zone 5 in the outcrop described in section 2, since there was no doubt that deformation was localized within this zone. The gouge was disaggregated by adding distilled water so as not to crush the coarse grains and change grain size distribution, and then its fine fraction (<106 μm) was extracted by using mesh cloth.

[13] Double shear frictional experiments were performed using a biaxial frictional testing machine at Kyoto University (Figure 6) (now at Hiroshima University) [*Kawamoto and Shimamoto*, 1997, 1998; *Shimamoto et al.*, 2006]. For the detailed description of the apparatus, please see section 4.1. Gabbro blocks were used as host rocks with a total displacement limited to 20 mm. The simulated fault surfaces were roughed by using grit 80 carborundum in order to prevent slip on the gouge-rock interface. The air-dried gouge sample was placed in two 1.5 g amounts on each "fault surface" of the two side blocks, and the three blocks were attached together to form the double-shear configuration. Then, distilled water was infiltrated into the gouge layers from one side by capillary action to avoid a situation where a dried area was surrounded by wet area. Previous works [e.g., *Morrow et al.*, 2000] show that absorbed water decreases frictional strength of fault gouge with clay minerals including smectite.

[14] The assembly of gabbro blocks with simulated faults was placed in the apparatus and compacted for more than 14 h (50,000 s) by applying 44.1 MPa normal stress prior to the actual experiment. Then, the normal stress was decreased to 29.4 MPa and we started applying shear stress. Velocity step tests were performed at load point velocities from 0.0154 to 155.54 μm s^{-1} at 29.4 MPa normal stress. During the experiments, the normal stress is kept approximately constant manually. The fluctuation in the normal stress is below 0.2% of the desired value. Velocity steps are performed by the combination of changes in the motor speed and the electric clutch for ones between 0.1554 and 1.54 μm s^{-1}, and by changing in the motor speed for the others. Note that these velocities are determined by the rate of revolution of the servo motor and the gear ratio, and used in the numerical fitting. There was no jacket around the specimen and some amount of gouge was squeezed out of the simulated fault when the normal stress was applied. In this sense, the thickness of the gouge layer is actually controlled by the applied normal stress, not solely by the amount of the gouge initially put in the simulated fault. Pore pressure is at atmospheric pressure if there is no rapid compaction or dilatation. During the experiments, a piece of paper was put around the simulated fault and kept wet so that water did not evaporate from the sample. The change in thickness of the gouge layer is also measured during the experiments. After the experiments, the thickness of gouge layer is approximately 200 μm under microscope (see the microphotographs in section 6). Assuming that this is equal to the final thickness in the experiment, accumulated averaged strain is calculated by integration of measured change in shear displacement divided by instantaneous thickness of a gouge layer given by measured change in thickness. Note that the measured shear displacement is not used in the inversion for the constitutive parameters since it has an electric noise and smoothing of it causes a problem at the point where a velocity step is performed. Because of the elastic deformation of apparatus, the absolute value of shear strain is not accurate, especially at the initiation of shear loading. Initial thickness of the simulated fault is approximately 250 μm. This is much thinner than used in the work

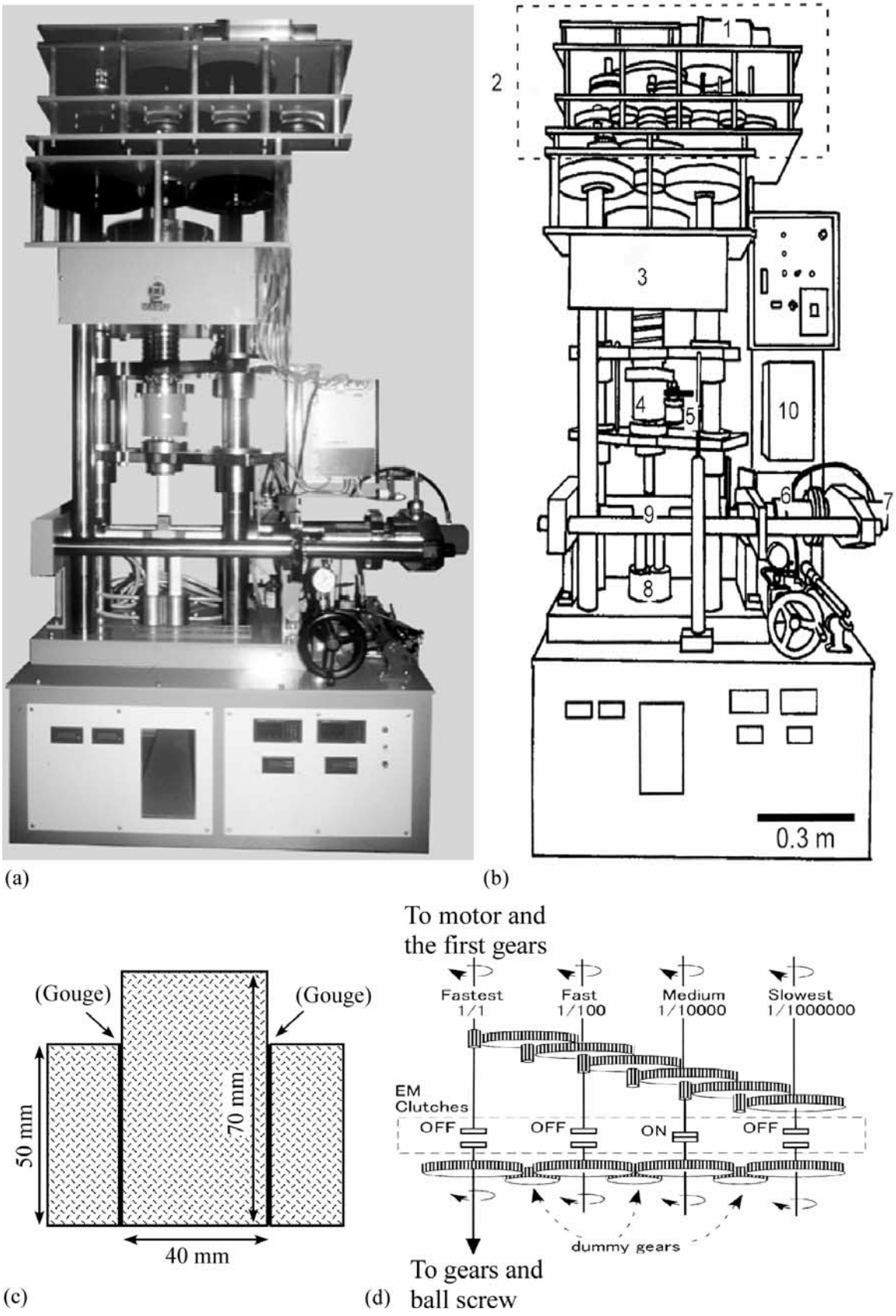
(a)
(b)
1
2
3
4
5
6
7
8
9
10
0.3 m
(c)
(Gouge)
(Gouge)
50 mm
70 mm
40 mm
(d)
To motor and
the first gears
Fastest
1/1
Fast
1/100
Medium
1/10000
Slowest
1/1000000
EM
Clutches
OFF
OFF
ON
OFF
dummy gears
To gears and
ball screw

Figure 6

by *Saffer and Marone* [2003] (initially 5 mm thick) for the mixture of smectites and quartz, and allows us to produce greater shear strain with restricted total displacement. The mechanical data were sampled by 2 or 5 Hz, and the resolution of the friction coefficient is about 10^{-6}. We conducted two runs (BAF045 and BAF046) with many velocity step tests in them at identical conditions so as to check the experimental reproducibility. The velocity steps are named BAF045-1 to -10 and BAF046-1 to -15 in order.

4. Apparatus-Fault Interaction and Inversion Technique

[15] In this section, we describe the apparatus used in detail and our inversion method for the fault constitutive parameters. Laboratory measurements of the constitutive parameters are not straightforward when conducting velocity step tests [e.g., *Tullis and Weeks*, 1986; *Reinen and Weeks*, 1993; *Blanpied et al.*, 1998] for variety of reasons. These include the fact that imposing approximately ideal step changes in slip rate is not always easy, subtle frictional properties can be obliterated by experimental issues such as O-ring friction and jacket strength, stick slip makes it almost impossible to determine the parameters including simply a steady state friction coefficient at a given slip rate, and the assumption of constant parameters may not be valid at a wide range of slip rates. Thus, not so many papers report complete sets of fault constitutive parameters [*Dieterich*, 1979, 1981; *Weeks and Tullis*, 1985; *Tullis and Weeks*, 1986; *Marone et al.*, 1990; *Blanpied et al.*, 1998; *Reinen et al.*, 1992, 1994; *Marone and Kilgore*, 1993; *Reinen and Weeks*, 1993; *Chester*, 1994; *Marone and Cox*, 1994; *Mair and Marone*, 1999; *Saffer and Marone*, 2003].

[16] In many testing machines the slip rate is controlled by prescribing displacement at a point away from a fault (the load point displacement), and in such cases the testing machine inevitably interferes with the fault motion even though load point velocity is changed in a stepwise manner. A testing machine always deforms elastically whenever the axial load or the frictional resistance along a fault changes, and hence the slip rate along the fault does not change in a stepwise manner. Given a stiffness value and a presumed form of the constitutive law, constitutive parameters can be determined by iterative numerical fitting with conducting many forward modelings of the apparatus-specimen interaction [*Reinen and Weeks*, 1993; *Reinen et al.*, 1994; *Chester*, 1994; *Marone and Cox*, 1994; *Blanpied et al.*, 1998; *Mair and Marone*, 1999; *Saffer and Marone*, 2003]. In principle, errors in the measurements of the constitutive parameters can be estimated statistically by using a variance-covariance matrix.

[17] A pitfall here is that the machine stiffness is implicitly treated as a constant without any error in many studies, and it is uncertain how much an error in stiffness measurement or fluctuation of stiffness affects the constitutive parameters. In other words, it is unclear if the true values of constitutive parameters are within the estimated errors if the uncertainty in the machine stiffness not considered properly. Testing machines have been treated as linearly elastic in such analyses. However, in practice, a testing machine consists of various mechanical elements and their junctions and thus behaves in complex manners resulting in changes in apparent stiffness value depending on the load levels or depending on how tightly the machine elements are pushed together. When a loading system consists of many machine elements such as pistons, spacers, gears, etc., some fluctuations of stiffness are inevitable, even under similar conditions. Thus, the effects of stiffness variation need to be evaluated in the measurements of constitutive parameters. *Blanpied et al.* [1998] treated the machine stiffness as a constant which varies for each velocity step. They estimated it from the rate of change in the friction directly after applying an abrupt change in the load point velocity and reported that it varies for about 10% for one step to another. In some apparatuses such as discussed by *Reinen and Weeks* [1993], the machine stiffness can actually be controlled by high-speed servo-control systems, in which case this issue might not be important.

[18] In order to show if the uncertainty of the fluctuation in the machine stiffness is important or not, we measure the stiffness of the apparatus and estimate the uncertainty in it. We then took a modeling approach where (1) we assumed a set of constitutive parameters, (2) we solved the apparatus-specimen interaction for an imposed load point velocity step to make a synthesized experimental data imposed with some random errors, and (3) then we analyzed the synthesized friction data, using the stiffness values which are different from the true value, to see if the originally assumed constitutive parameters can be recovered or not.

4.1. A Biaxial Frictional Testing Machine

[19] We have used a high-temperature, wide-velocity biaxial frictional testing machine (Figure 6), reported by *Kawamoto and Shimamoto* [1997, 1998]. The machine was designed to study frictional properties of faults at temperatures to about 1,000°C over slip rates ranging from 1.5 mm s^{-1} down to 0.05 mm a^{-1}. The experiments shown in this paper were conducted at room temperature, but a split furnace with Kanthal heating wire can be used for high-temperature dry friction experiments. This was used, for example, in halite shearing experiments from brittle

Figure 6. (a) A photograph and (b) schematic sketch of a biaxial frictional testing machine produced by Marui Co. Ltd. (MIS-0233-1-302), (c) a three-block specimen assembly with or without gouge, and (d) an automatic gear-change system with electromagnetic clutches. Numbers in Figure 6b denote 1, servo-motor; 2, gear-change system shown in Figure 6d; 3, ball screw; 4, axial force gauge; 5, displacement transducer; 6, normal force gauge; 7, hydraulic jack for applying normal force; 8, water-circulating chamber for cooling of the pistons; 9, specimen assembly shown in Figure 6c; and 10, controller of servo-motor. The central and side blocks are 40 × 40 × 70 mm and 20 × 40 × 50 mm in sizes, respectively, allowing 20 mm in maximum displacement.

to fully plastic regimes [see *Kawamoto and Shimamoto*, 1997, Figure 1]. Changes in the slip rates by over 9 orders of magnitudes was attained by a gear-train system equipped with a servo-motor and a ball screw converting rotary motion into axial displacement. The rate of revolution of the servo-motor can be varied by 3 orders of magnitude with a maximum of 4,000 rpm. The gear train system has four sets of gear assemblies, i.e., the fastest, fast, medium and slowest assemblies as shown schematically in Figure 6d (see the second and the third chambers from the top of gear assembly in Figures 6a and 6b). The rate of revolution is decreased 100 times by two sets of 10:1 gears from one assembly to the next slow assembly (upper gears in Figure 6d), the rotary motion is returned to the fastest line by a series of dummy gears (lower gears in Figure 6d). Thus, the gear assemblies can produce a speed change by up to 6 orders of magnitude, and totaling 9 orders when combined with motor speed. The gear assembly can be changed by using four sets of electromagnetic clutches. For instance, the clutch at medium rate is connected while others are disconnected in Figure 6d, and the medium-speed gear assembly is then selected. A speed-controlling lever allows those clutches to be turned off and on almost instantly without stopping the motor. The displacement rate can be varied in a stepwise manner by any amount within these 9 orders of magnitude either by changing the motor speed or by changing the clutch combinations. Thus, the machine is suitable for the velocity step experiments to study frictional properties of faults.

[20] Specimen assembly consists of the central block of 40 mm × 40 mm × 70 mm in size and of two side blocks of 20 × 40 × 50 mm in size, with or without gouge layers in between (Figure 6c). This assembly allows for a maximum displacement of 20 mm. With this direct shear arrangement, the motor-and-gear vertical loading system and a horizontal hydraulic ram independently control the shear and normal stresses, respectively, on the sliding surfaces between blocks. The axial and normal force gauges have capacity of 500 and 200 kN, respectively, corresponding to a maximum normal stress of about 100 MPa. More details of the specimen assembly for high-temperature experiments are given by *Kawamoto and Shimamoto* [1997, 1998].

[21] The advantages of our biaxial machine are as follows. High accuracy in the measurement of friction is attained because no jacket is used around specimen; this is important in studying subtle rate- and state-dependent friction. The use of motor/gear/electromagnetic clutch assembly has enabled step changes in the slip rate over large ranges, the slowest rate being far below tectonic plate velocity. This slow rate capability will be useful for studying slow processes such as solution/precipitation creep along faults. A pressure vessel is made for conducting friction experiments with the three-block assembly although it is not used in this work.

[22] A disadvantage of the machine is that only the load point velocity or the rate of revolution of the motor can be controlled, and there is no feedback control of the slip rate of simulated faults. Thus, analysis of specimen-apparatus interaction is essential for accurate determination of fault constitutive parameters.

4.2. Mechanical Behavior Just After a Velocity Step

[23] In this work, we use fault constitutive equations with the aging law [*Dieterich*, 1979] and the slip law [*Ruina*, 1983] which can be written in a derivative form:

$$\Delta\dot{f} = a\frac{\dot{V}}{V} + b\frac{\dot{\theta}}{\theta}, \tag{1}$$

$$\text{Slip law}\quad \dot{\theta} = -\frac{V\theta}{d_c}\ln\left(\frac{V\theta}{d_c}\right), \tag{2}$$

$$\text{Aging law}\quad \dot{\theta} = 1 - \frac{V\theta}{d_c}, \tag{2'}$$

where overdots represent time derivative, Δf is the change in the frictional coefficient from the initial value, V is the slip rate of a fault, and θ is the state variable describing the change in friction with the characteristic distance, d_c. The constitutive parameter a gives the instantaneous response of the friction upon a step change in slip rate, and the change in the steady state friction f_{ss} with respect to the logarithm of the slip rate is given by $(a-b)(= df_{ss}/d\ln V)$.

[24] We do prefer the derivative form to the standard integrated form $f = f_0 + a\ln(V/V_0) + b\ln(V_0\theta/d_c)$. Many previous studies indicate that [e.g., *Logan and Rauenzahn*, 1987; *Mair and Marone*, 1999] b and d_c varies with slip rate, V. But if we write them as a function of V, the third term in the standard form gives direct effect, which is contrary to the idea of the separation of the direct and evolution effects in formulating rate- and state-dependent law in the current form. We think the separation of the direct effect and the evolution effect is more important than the appearance of the integrated form. In the derivative form, b and d_c are allowed to be a function of V.

[25] Experimental data are often fit better with two state variables [e.g., *Blanpied et al.*, 1998]:

$$\Delta\dot{f} = a\frac{\dot{V}}{V} + b_1\frac{\dot{\theta}_1}{\theta_1} + b_2\frac{\dot{\theta}_2}{\theta_2}, \tag{3}$$

$$\text{Slip law}\quad \dot{\theta}_i = -\frac{V\theta_i}{d_{ci}}\ln\left(\frac{V\theta_i}{d_{ci}}\right)(i = 1, 2), \tag{4}$$

$$\text{Aging law}\quad \dot{\theta}_i = 1 - \frac{V\theta_i}{d_{ci}}(i = 1, 2). \tag{4'}$$

The second state variable was introduced in order to fit the numerical model to the experimental data. The need of more than one state variable may indicate the existence of several physical processes operating at the frictional surface, or just a defect in the form of the constitutive law of a fault; for example, a frictional behavior predicted by the slip law with one state variable cannot be explained perfectly by the aging law with one state variable.

[26] Velocity step tests are often performed to determine the frictional constitutive parameters a, b and d_c, or a, b_1, b_2, d_{c1} and d_{c2} by conducting numerical curve fitting with

those equations. However, good fitting does not warrant the determination of the constitutive parameters when the stiffness of machine, k ([1/(length)], and the change in the friction coefficient per unit shortening of the spring) is not determined accurately, or fluctuates from one test to the other. To explore the apparatus-fault interaction upon a velocity step, let us consider the case where the evolution in θ is negligibly small, corresponding to the case: $d_c \to \infty$. Suppose that the steady state is achieved before a velocity step at slip rate of V_0, and that the loading velocity is abruptly changed to U at $t = 0$. From the logarithmic rate dependency of the instantaneous term a, the change in frictional coefficient before and after the velocity step is given by

$$\Delta\dot{f} = a\frac{\dot{V}}{V}. \tag{5}$$

From the elastic deformation of the apparatus, the change in frictional coefficient is also given by

$$\Delta\dot{f} = k(U - V). \tag{6}$$

Equations (5) and (6) yield a nonlinear ordinary differential equation:

$$\dot{V} = -\frac{k}{a}\left(V - \frac{U}{2}\right)^2 + \frac{kU^2}{4a}. \tag{7}$$

Equation (7) can be solved by a coordinate transformation:

$$\xi = \tanh^{-1}\left(\frac{2V}{U} - 1\right), \tag{8}$$

and the general solution for V is

$$V = \begin{cases} \dfrac{U}{2}(1 + \tanh(t/(2a/kU) + C)) & (U > V_0) \\ \dfrac{U}{2}(1 + \coth(t/(2a/kU) + C)) & (U < V_0) \end{cases}, \tag{9}$$

where C is a real integration constant to be determined by the initial condition:

$$V_0 = \begin{cases} \dfrac{U}{2}(1 + \tanh(C)) & (U > V_0) \\ \dfrac{U}{2}(1 + \coth(C)) & (U < V_0) \end{cases}. \tag{10}$$

Equation (10) shows an interesting feature that the shape of $V(t)$ to the peak frictional coefficient is different between positive and negative velocity steps.

[27] If the amount of displacement from $t = 0$ to the peak friction coefficient is negligibly small compared to d_c, (10) holds approximately even for the full system with a finite d_c exhibiting state evolution. In such a case, the scales of the slip displacement before and after the peak are separated, and the height of the peak is determined by a alone and not affected by the value of k, like in an ideal step in V. At this limit, the uncertainty in k hardly affects the evolution in Δf and thus the optimum values for the constitutive parameters in the numerical fitting. Otherwise, the state evolution affects Δf until the peak with rounding and shortening it. In this situation, the fitting of Δf even before the peak is important, and thus, the error in k can propagate to the estimate of the constitutive parameters.

[28] For positive velocity step, the slip rate is often increased by a factor of 10 [e.g., *Blanpied et al.*, 1998]. In this case, (10) yields $C = 1.099$, and time evolution of the friction coefficient and slip rate predicted by (5) or (6) and (9) are shown in Figures 7a and 7c. The initial steep increase in the friction coefficient due to the direct effect is almost complete at about $t = 4a/kU$. From (9), the slip displacement at that time, d_a, is given by

$$d_a = \int_0^{4a/kU} V dt = 1.850\frac{a}{k} \approx \frac{2a}{k}(U = 10V_0). \tag{11}$$

In the negative velocity step tests, the slip rate is often decreased by a factor of 10. In this case, (10) yields $C = 5.268 \times 10^{-2}$, and time evolution of the frictional coefficient and the slip rate are shown in Figures 7b and 7d. Compared with the case of positive velocity step, the initial drop in the frictional coefficient is more rapid and the initial rapid change is almost complete at about $t = 2a/kU$. Slip displacement from $t = 0$ to this point is

$$d_a = \int_0^{2a/kU} V dt = 4.173\frac{a}{k} \approx \frac{4a}{k}(U = 0.1V_0). \tag{12}$$

It is interesting that d_a in the positive velocity step is about twice as large as that in the negative velocity step. This probably indicates that the initial behavior prior to the peak friction is affected more easily by the state evolution with short d_c in positive velocity steps than in negative ones. Note that the specific form of the state evolution equation (e.g., the aging law [*Dieterich*, 1979] or the slip law [*Ruina*, 1983]) does not matter in the discussion presented in here.

4.3. Uncertainty in the Machine Stiffness

[29] We now look at the real stiffness of the biaxial friction apparatus in Figure 6. Figure 8a shows a schematic diagram showing the constitution of machine elements in the apparatus. Without changing the stiffness (or decrease in shear loading per unit slip on the simulated fault), Figure 8a can be redrawn to Figure 8b. We measured the stiffness of the pistons and specimen in series by measuring the change in length of the assembly upon load cycling, using a solid specimen without faults. Figure 9 is an example of shear loading plotted against the measured displacement with a rigid gabbro block as a specimen. Note that inelastic deformation (probably, time-dependent adjustments of machine elements at their junctions) takes place upon the load cycling and that the limiting nearly elastic behavior is highly nonlinear with respect to load and displacement. The apparent stiffness (or the slope of load displacement curve) at around 25 kN shear loading increases from 0.866×10^{-8} N m^{-1} at the initial cycle to the limiting value of 1.69×10^{-8} N m^{-1} after several cycles. Such complex stiffness properties are not desirable for a testing

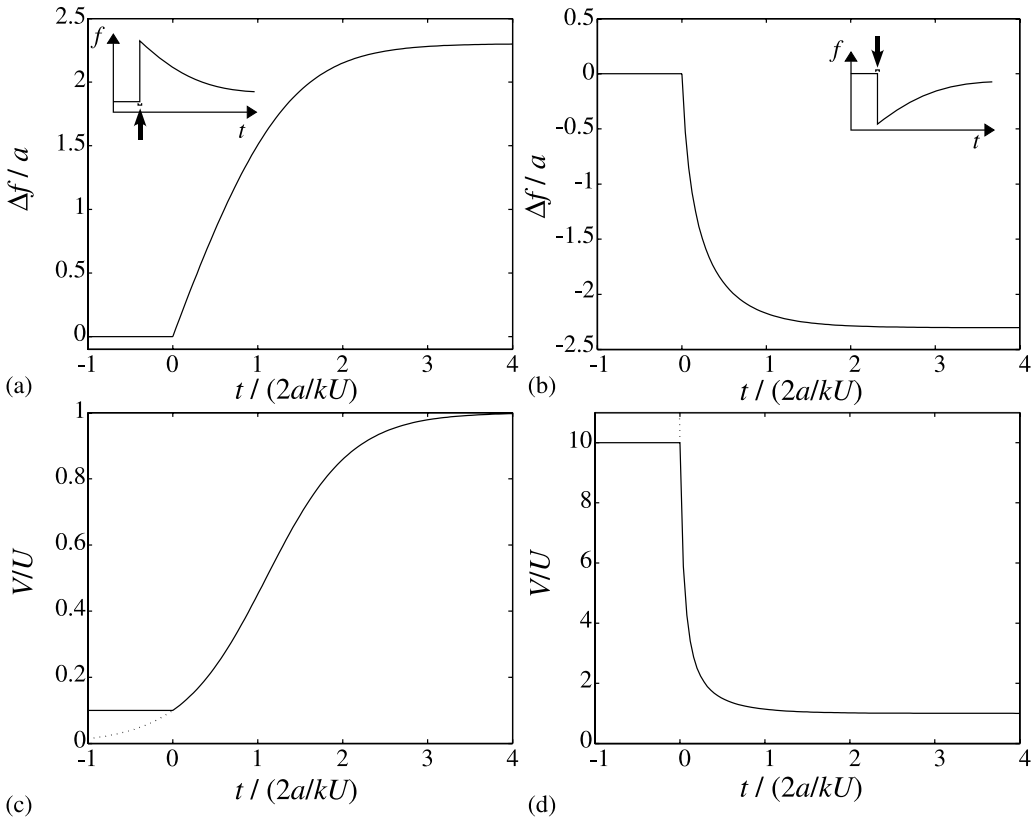

Figure 7. Change in (a and b) frictional coefficient and (c and d) slip rate just after a positive (Figures 7a and 7c) and negative (Figures 7b and 7d) velocity step. Slip rate changes in a shape of tanh and coth function, respectively.

machine, but are inevitable because machine elements are assembled loosely and their junctions behave in complex manner upon loading. The stiffness properties may be improved by imposing initial contraction to the assembly.

[30] The stiffness of the press and loading system in series can be estimated by measuring the drop in axial load and the displacement during stick-slip events, under an assumption that the load point displacement is negligibly small during each stick-slip event [e.g., *Shimamoto et al.*, 1980]. This assumption is justified because stick-slip events occur in the time scale of milliseconds and the external loading rate is small (about 0.5–30 μm s^{-1}). The stress drop is controlled by the load point velocity by changing the revolution rate of the servo-motor and electric clutch. We tested the fastest and the second fastest gear lines (see Figure 6d) which are used in the actual friction experiments presented in this paper. The stiffness is not affected by the gear lines since a single line explains the two sets of data plotted in Figure 10. The result shown in Figure 10 yields a stiffness of 2.03 ± 0.02 × 10^{-8} N m^{-1}. It should be emphasized that the data points scatter widely although the optimum value can be determined accurately. Given a single stick-slip event, we have to assume a stiffness value which differs from the optimum value by tens of percents to explain it. This is also true for several previous studies on stick-slip experiments such as shown in Figure 14 of *Ohnaka* [1973] and Figure 9 of *Shimamoto et al.* [1980].

[31] These two stiffnesses give total stiffness of the apparatus that range from 0.605 × 10^8 to 0.864 × 10^8 N m^{-1}.

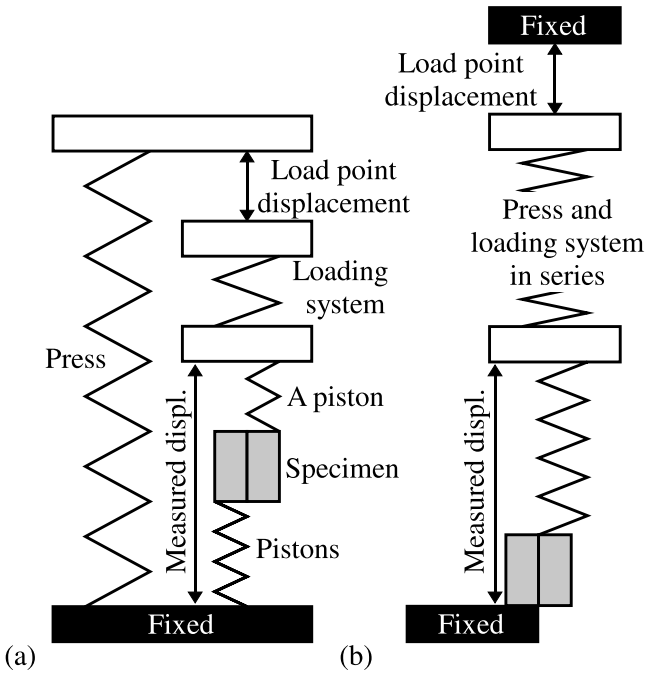

Figure 8. (a) A schematic diagram and (b) its interpretation of a biaxial frictional apparatus.

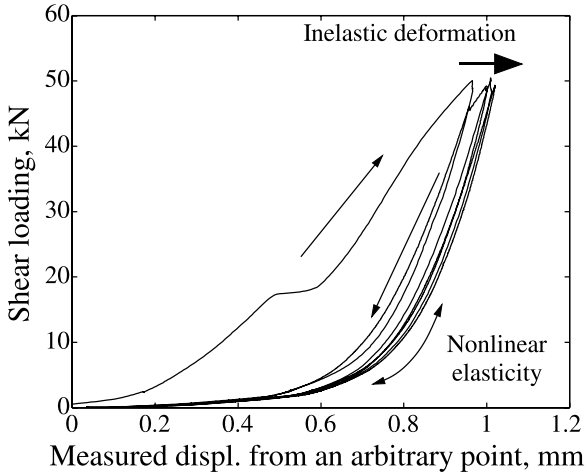

Figure 9. Shear loading plotted against measure displacement (Figure 8) with a specimen without a simulated fault. Inelastic deformation of the apparatus takes place, and the limit behavior is nonlinearly elastic.

If we take the central value, 0.735×10^8 N m^{-1} as a most likely stiffness, the estimate of error in stiffness is about 18%. Note that k is the stiffness value reported here divided by 2 times the normal load since there is 2 simulated faults in the double-shear configuration. Intuitively, the amount of uncertainty is not small, and it is important to evaluate if this is critical or not in the determination of constitutive parameters. Section 5 attempts this evaluation.

4.4. Significance of Stiffness Fluctuation in Determining the Constitutive Parameters

4.4.1. Synthesized Friction Data

[32] Real laboratory data from friction experiments cannot be used for evaluating if the fitting is successful or not since one can never know the true answer. Thus, we conduct numerical modeling by starting from known constitutive parameters to synthesize an experimental data and analyze the synthesized data set with false stiffness values to evaluate whether or not preassigned parameters can be recovered.

[33] The data used here were artificially produced by using a constitutive law of equations (1) and (2) (slip law), combined with analyzing linearly elastic deformation of the apparatus, expressed by equation (6). We also tested the Aging law (equation (2′)), but the conclusion is same as in the cases with Slip law and thus not presented here. We need to systematically make a series of synthesized data to compare the results since the resulting parameters and their covariance matrices are affected by experimental conditions such as the number of data points, the total displacement compared to d_c, and the noise level. A set of differential equations (equations (1), (2), and (6)) can be expressed in terms of a/k as a length scale and U as a velocity scale (and thus a/kU as a time scale):

$$\overset{\circ}{\Delta f} = a(\varsigma - 1), \tag{13}$$

$$\overset{\circ}{\Delta f} = a\frac{\overset{\circ}{\varsigma}}{\varsigma} + b\frac{\overset{\circ}{\phi}}{\phi}, \tag{14}$$

$$\overset{\circ}{\phi} = -\frac{\varsigma\phi}{\delta_c}\ln\left(\frac{\varsigma\phi}{\delta_c}\right), \tag{15}$$

where open circles on top represent nondimensional time derivative, $d/d(t \cdot kU/a)$, $\varsigma = V/U$, $\phi = \theta \cdot (kU/a)$, and $\delta_c = d_c/(a/k)$.

[34] Equations (13) to (15) shows that the shape of resulting frictional coefficient as a function of nondimensional time depends only on a, b, and δ_c. Moreover, the shape depends only on b/a and δ_c, if the change in frictional coefficient is normalized by a. For simplicity, we use one state variable with $a = b = 0.01$ ($a/b = 1$), and tested 3 cases, $\delta_c = 100$, 10, and 1. The initial condition was set as $\varsigma_0 = 0.1$ and $\varsigma_0 = 10$ for velocity increments and decrements by a factor of 10, respectively. Before a velocity step, a steady state ($f_{ss} = 0.7$) is assumed to be achieved. In a real experiment, we tend to wait until the steady state frictional coefficient at the next slip rate is recognized by eye, and the sampling frequency is chosen for the experimentalist's convenience; people tend to choose the sampling interval in order to resolve d_c. Therefore, the numerical velocity step experiments last until the nondimensional slip displacement or time, Utk/a reaches 10 δ_c. The synthesized data have 10,000 points after an applied velocity step and points before it. All experimental data thus synthesized were superposed with random noise described by the Gaussian distribution with a standard deviation of 0.0001. This value is comparable to a typical electric noise level in our experiments at a normal stress about 30 MPa as shown later. *Reinen and Weeks* [1993] showed that adding extra noise makes determination of the parameters easier because of the

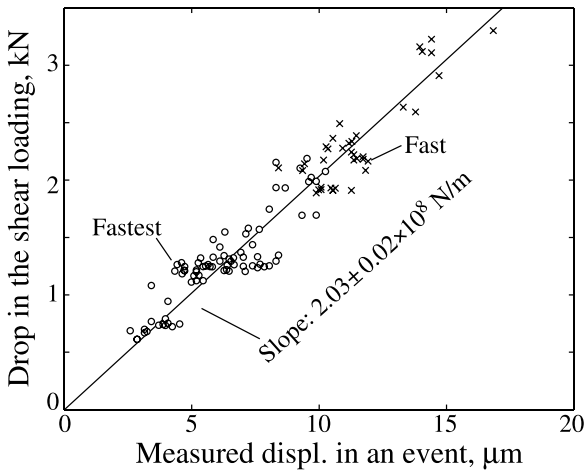

Figure 10. Measured slip displacement and drop in shear loading obtained from stick-slip experiments around shear loading of 25 kN. The drop in the shear stress loading is larger at a smaller loading velocity which ranges from about 0.5 to 30 μm s^{-1}. Two of the gear lines, fastest (open circles) and fast (crosses) in Figure 6 are tested.

increase in variances. But in this study, we would like to pursue the accurate determination of the parameters.

[35] Many experimental data upon velocity steps are better fit by using a constitutive law, am equation with two state variables [e.g., *Blanpied et al.*, 1998] (equations (3) and (4)). It is thus important to evaluate the effect of stiffness fluctuation in determination of those two state variables. Equations (3) and (4) can be rewritten in after nondimentionalization:

$$\overset{\circ}{\Delta f} = a\frac{\overset{\circ}{\varsigma}}{\varsigma} + b_1\frac{\overset{\circ}{\phi_1}}{\phi_1} + b_2\frac{\overset{\circ}{\phi_2}}{\phi_2} \tag{16}$$

$$\overset{\circ}{\phi_i} = -\frac{\varsigma\phi_i}{\delta_c}\ln\left(\frac{\varsigma\phi_i}{\delta_c}\right). \tag{17}$$

The synthesized experimental data for a two-state variable case were produced in the same manner as for the one-state variable cases. We also test a positive velocity step by a factor of 10 with $\delta_{c1} = 1$, $\delta_{c2} = 10$, $a = 0.01$, and $b_1 = b_2 = 0.005$, and total data length is $10\delta_{c2}$.

[36] In the numerical simulations both in creating a synthesized data and in the least squares fitting, the Runge-Kutta-Fehlberg (RKF) 45 method [*Fehlberg*, 1969] is used with adaptive time steps if needed. The acceptable error level is set as 10^{-10} in Δf for a single time step, but the actual numerical error is probably much smaller since the integration scheme uses local extrapolation. Thus, the numerical error after 10,000 steps is much smaller relative to the parameters to be determined such as a and b which are around 0.01. Numerical fitting to these artificially synthesized experimental data is conducted with three sets of stiffness values: the correct stiffness value and higher and lower stiffness values each by 10%.

4.4.2. Inversion Technique

[37] At the beginning of forward modeling, we determined the optimum time for the abrupt step in the load point velocity from the subset of the data just after the velocity step. This process improves the fitting of the initial part from the velocity step to the peak value of Δf. We solved iteratively the least squares problem with a bisection line search method since the parameter apace is just one-dimensional. In the real experiments, there often is a global trend such as displacement hardening behavior. This trend is assumed to be a function of the load point displacement and estimated by using a second-order polynomial for each velocity step based on the averaged rates of change in the friction coefficient in regions where we recognize the steady state. This procedure is inside the iteration for determining the step time. No global trend is assumed in the analyses of the synthesized data presented in this section.

[38] In solving the least squares problem for the set of constitutive parameters, a uniform weight function for all data points is used to avoid additional complexity. Just note that the decaying weight function often used in this kind of analyses [e.g., *Reinen and Weeks*, 1993] probably emphasizes the effect of uncertainty in k since the data points before the peak is highly affected by the value of k. We used the Levenberg-Marquardt method with a damping controller by *Nielsen* [1999]. A possible update in the parameter vector $\mathbf{P}$ is given by

$$\Delta\mathbf{P} = \left(\mathbf{J}^{\mathrm{T}}\mathbf{J} + \mu\mathbf{I}\right)^{-1}\mathbf{J}^{\mathrm{T}}\left(\mathbf{f}_{\mathrm{pred}} - \mathbf{f}_{\mathrm{obs}}\right), \tag{18}$$

where $\Delta\mathbf{P}$ is the update to $\mathbf{P}$, $\mathbf{f}_{\mathrm{obs}}$ and $\mathbf{f}_{\mathrm{pred}}$ are vectors containing observed and predicted friction coefficient histories, and $\mathbf{J}$ is the derivative of $\mathbf{f}_{\mathrm{pred}}$ with respect to the parameters, $\mathbf{P}$. μ is the damping parameter. If μ is zero, $\Delta\mathbf{P}$ is identical to one given by the Gauss-Newton method, and if μ is very large, $\Delta\mathbf{P}$ becomes a short vector in the steepest decent direction. For every possible update we calculated the gain ratio:

$$\rho = \frac{S(\mathbf{P}) - S(\mathbf{P} + \Delta\mathbf{P})}{L_{\mathbf{P}}(\mathbf{P}) - L_{\mathbf{P}}(\mathbf{P} + \Delta\mathbf{P})}, \tag{19}$$

where S is the summation of the squared differences and $L_{\mathbf{P}}$ is the approximation of S based on the linearization of $\mathbf{f}_{\mathrm{pred}}$ around $\mathbf{P}$. Large ρ indicate that the linear approximation to $\mathbf{f}_{\mathrm{pred}}(\mathbf{P})$ is good, so that we can decrease μ:

$$\mu := \mu \cdot \max\left\{1/3, 1 - (2\rho - 1)^3\right\},\ \nu := 2\ (\text{if } \rho > 0); \tag{20}$$

ν is a number controlling the increase in μ, and initialized in a successful update. The denominator in (19) is always positive if our numerical derivative is accurate enough. Then, if ρ is negative or zero, we have to reject the update, and solve (18) for the new possible update after increasing μ:

$$\mu := \mu \cdot \nu,\ \nu := 2\nu\ (\text{if } \rho \le 0). \tag{21}$$

We iterate the search for the optimum values of the constitutive parameters until the components of the update becomes less than 1% of each standard deviation. The variance-covariance matrices normalized by the optimum value of the parameters are also reported so that the half length of an error bar (2σ) relative to the optimum parameter value is twice the square root of the corresponding diagonal component.

4.4.3. Least Squares Fitting With Prescribed Machine Stiffness

[39] In this section, we present a fitting result to the synthesized experimental data. The fault constitutive parameters (a, b, d_c, and initial value of f, f_i) are treated as the unknown parameters, and a fixed value of k is prescribed. Figures 11 and 12 present the synthesized experimental data with one state variable and the best fit curves in positive and negative velocity steps, respectively. We plotted them with the number of data points as the y axis because the load point displacement is slightly different for the cases plotted. The mismatch between the true answer and the optimum parameter values are listed in Table 1 (positive step) and in Table 2 (negative step) after normalizing by the optimum parameter values. The length of the error bar or twice the standard deviation, 2σ, and the variance-covariance matrices are also tabulated. If 2σ is smaller than the absolute value of a corresponding parameter, we failed to recover the true answer as footnoted in Tables 1 and 2. With $\delta_c = 100$,

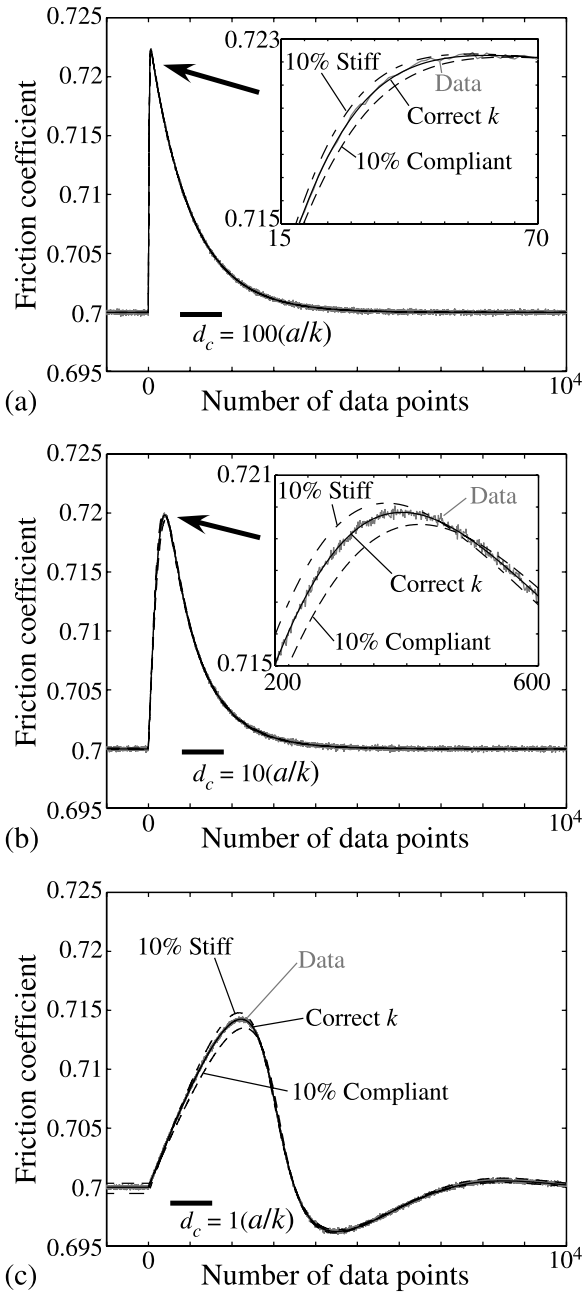

Figure 11. Synthesized experimental data of positive velocity steps by a factor of 10 and the best fit curves to them with (a) $\delta_c = d_c/(a/k) = 100$, (b) $\delta_c = 10$, and (c) $\delta_c = 1$. Two dashed lines represent the best fit curves with 10% higher and lower values of the stiffness of the apparatus, k.

we sometimes succeeded in recovering the true answer with wrong stiffness values. Even if we failed, the mismatch is larger than 2σ at most a factor of 2. This indicates that the uncertainty in the apparatus stiffness is important in determining the constitutive parameters, but the estimated optimum parameter values and their error bar are not bad if d_c is much longer than a/k. On the other hand if δ_c is 10 or smaller, all of the relative mismatches from the true answer with a wrong stiffness values are larger than 2σ sometimes by more than one order of magnitude. In these cases, deviation of the least squares solution from real constitutive parameters due to wrong stiffness is so large that the optimum values and their error bars do not give the correct estimates of the constitutive parameters. Given that the stiffness of an apparatus may well change by several percent during an experiment due to inelastic deformation, it is difficult to determine the constitutive parameters unless δ_c is orders of magnitude greater than unity.

[40] Figure 13 shows the synthesized experimental data with two state variables and the least squares fittings to the data, and Table 3 gives the mismatches of thus determined constitutive parameters from their true values, 2σ, and their

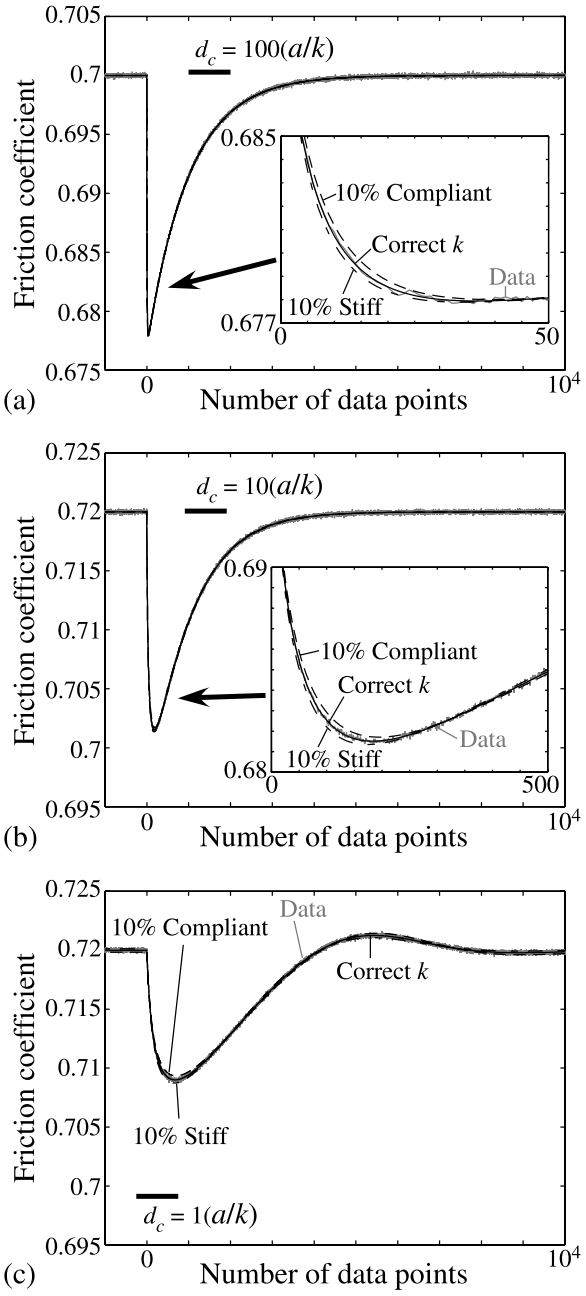

Figure 12. Synthesized experimental data of negative velocity steps by a factor of 10 and the best fit curves to them with (a) $\delta_c = d_c/(a/k) = 100$, (b) $\delta_c = 10$, and (c) $\delta_c = 1$. Two dashed lines represent the best fit curves with 10% higher and lower values of the stiffness of the apparatus, k.

Table 1. Fitting Results to Positive Velocity Steps[a]

	Mismatch	2σ	Variance-Covariance Matrix			
			a	b	d_c	f_i
			$\delta_c = 100$			
Compliant						
a	−1.1E-3	6.6E-4[b]	1.1E-7	8.4E-8	−9.9E-8	−7.2E-10
b	−1.1E-3	5.8E-4[b]		8.4E-8	−8.4E-8	−3.1E-12
d_c	3.6E-4	9.5E-4			2.3E-7	1.1E-11
f_i	2.2E-6	9.7E-6				2.3E-11
Correct stiffness						
a	−1.0E-4	6.2E-4	9.7E-8	7.5E-8	−8.8E-8	−6.3E-10
b	−2.1E-4	5.5E-4		7.5E-8	−7.5E-8	−1.2E-12
d_c	9.6E-5	9.0E-4			2.0E-7	8.8E-12
f_i	−2.1E-6	1.1E-6				2.1E-11
Stiff						
a	5.6E-4	6.5E-4	1.1E-7	8.2E-8	−9.6E-8	−6.9E-10
b	4.4E-4	5.7E-4		8.2E-8	−8.2E-8	−3.3E-12
d_c	−1.8E-5	9.4E-4			2.2E-7	8.1E-12
f_i	−4.2E-6	9.5E-6				2.3E-11
			$\delta_c = 10$			
Compliant						
a	−1.3E-2	1.1E-3[b]	3.0E-7	2.2E-7	−2.6E-7	−2.2E-09
b	−1.2E-2	9.3E-4[b]		2.1E-7	−2.1E-7	−8.5E-11
d_c	−6.3E-3	1.5E-3[b]			5.7E-7	4.5E-10
f_i	8.8E-5	1.7E-5[b]				6.9E-11
Correct stiffness						
a	−2.3E-4	5.8E-4	8.5E-8	6.2E-8	−7.6E-8	−6.4E-10
b	2.5E-4	5.0E-4		6.2E-8	−6.1E-8	−2.1E-11
d_c	−3.2E-5	8.1E-4			1.7E-7	1.2E-10
f_i	1.3E-6	9.0E-6				2.0E-11
Stiff						
a	8.9E-3	9.9E-4[b]	2.5E-7	1.8E-7	−2.2E-7	−1.9E-09
b	7.6E-3	8.5E-4[b]		1.8E-7	−1.8E-7	−5.4E-11
d_c	7.6E-3	1.4E-3[b]			4.9E-7	3.2E-10
f_i	−6.8E-5	1.5E-5[b]				6.0E-11
			$\delta_c = 1$			
Compliant						
a	−5.8E-2	2.2E-3[b]	1.2E-6	8.3E-7	−1.8E-6	−1.1E-08
b	−4.8E-2	1.6E-3[b]		6.4E-7	−1.1E-6	−4.7E-09
d_c	−4.6E-2	3.4E-3[b]			2.9E-6	1.5E-08
f_i	4.7E-4	2.7E-5[b]				1.9E-10
Correct stiffness						
a	−2.0E-9	6.4E-4	1.0E-7	6.3E-8	−1.1E-7	−1.1E-09
b	−3.6E-9	4.2E-4		4.4E-8	−7.0E-8	−5.4E-10
d_c	−4.5E-9	7.8E-4			1.5E-7	1.1E-09
f_i	−7.6E-6	8.9E-6				2.0E-11
Stiff						
a	5.8E-2	1.3E-3[b]	4.2E-7	3.2E-7	−6.5E-7	−2.9E-09
b	4.1E-2	1.1E-3[b]		2.8E-7	−4.3E-7	−1.1E-09
d_c	4.0E-3	2.2E-3[b]			1.2E-6	5.3E-09
f_i	−7.6E-4	1.6E-5[b]				6.6E-11

[a]See Figure 11. All numbers are normalized by the optimum parameter values.
[b]True answer not recovered.

variance-covariance matrix. We successfully recover the true answer with the correct stiffness, whereas with the overestimated or underestimated stiffness values the relative mismatches from the true answer are larger than the estimated errors. These results indicate that the accurate determination of the machine stiffness prior to an experiment is essential in determining the optimum parameter values and their errors correctly if we treat the stiffness as a fixed constant. This is especially true if the relative mismatch in the parameters associated with the shorter d_c are very large. Note that for all cases, the fitting looks great at least graphically (Figures 11, 12, and 13).

4.5. Least Squares Fitting With Stiffness as a Fitting Parameter

[41] Numerical modeling in section 4.4 clearly demonstrated that incorrect or fluctuating stiffness values cause nonnegligible errors in the estimate of constitutive parameters. On the other hand, the stiffness variation is due primarily to complex interactions of machine elements at their junctions and is difficult to control. To overcome this difficulty, we propose here to treat the stiffness of the apparatus as a fitting parameter assuming that the stiffness is constant during each velocity step experiment. The fitting procedures are the same as those in section 4.4.1, except that there is one more unknown parameter, k. Table 4 shows

Table 2. Fitting Results to Negative Velocity Steps[a]

	Mismatch	2σ	Variance-Covariance Matrix			
			a	b	d_c	f_i
			$\delta_c = 100$			
Compliant						
a	3.8E-4	6.5E-4	1.1E-7	8.2E-8	−9.6E-8	6.7E-10
b	7.3E-4	5.7E-4[b]		8.1E-8	−8.2E-8	1.1E-11
d_c	−1.7E-3	9.3E-4[b]			2.2E-7	−1.4E-11
f_i	−9.4E-6	9.3E-6[b]				2.2E-11
Correct stiffness						
a	−3.6E-4	6.4E-4	1.0E-8	7.9E-8	−9.3E-8	6.4E-10
b	−6.0E-5	5.6E-4		7.9E-8	−8.0E-8	1.2E-11
d_c	1.1E-4	9.1E-4			2.1E-7	−1.3E-11
f_i	−5.0E-6	9.1E-6				2.1E-11
Stiff						
a	−1.0E-3	6.5E-4[b]	1.0E-7	8.1E-8	−9.5E-8	6.6E-10
b	−7.1E-4	5.7E-4[b]		8.1E-8	−8.1E-8	1.1E-11
d_c	1.4E-3	9.2E-4[b]			2.1E-7	−1.0E-11
f_i	−3.1E-6	9.2E-6				2.1E-11
			$\delta_c = 10$			
Compliant						
a	6.1E-3	8.2E-4[b]	1.7E-7	1.3E-7	−1.6E-7	9.7E-10
b	6.4E-3	7.1E-4[b]		1.3E-7	−1.4E-7	1.6E-10
d_c	−1.5E-2	1.1E-3[b]			3.1E-7	−1.6E-10
f_i	3.1E-5	1.0E-5[b]				2.7E-11
Correct stiffness						
a	−1.0E-4	7.0E-4	1.2E-7	9.6E-8	−1.1E-7	7.1E-10
b	−1.3E-4	6.1E-4		9.2E-8	−9.8E-8	1.0E-10
d_c	−7.7E-5	9.5E-4			2.2E-7	−1.1E-10
f_i	6.1E-7	5.9E-6				2.0E-11
Stiff						
a	−5.7E-3	7.7E-4[b]	1.5E-7	1.2E-7	−1.3E-7	8.7E-10
b	−5.9E-3	6.7E-4[b]		1.1E-7	−1.2E-7	1.2E-10
d_c	1.2E-2	1.1E-3[b]			2.8E-7	−1.2E-10
f_i	2.6E-5	1.0E-5[b]				2.5E-11
			$\delta_c = 1$			
Compliant						
a	9.1E-3	2.1E-3[b]	1.1E-6	8.9E-7	−9.7E-7	5.0E-09
b	1.3E-2	1.8E-3[b]		7.8E-7	−8.3E-7	2.9E-09
d_c	−5.8E-2	2.2E-3[b]			1.1E-6	−3.1E-09
f_i	−2.3E-4	1.6E-5[b]				6.5E-11
Correct stiffness						
a	−4.4E-4	1.0E-3	2.7E-7	2.2E-7	−2.5E-7	1.3E-09
b	−5.3E-4	8.9E-4		2.0E-7	−2.1E-7	7.4E-10
d_c	4.3E-4	1.1E-3			3.2E-7	−7.5E-10
f_i	3.0E-6	8.6E-6				1.9E-11
Stiff						
a	−1.9E-2	1.7E-3[b]	7.4E-7	6.1E-7	−6.7E-7	3.6E-09
b	−2.2E-2	1.5E-3[b]		5.4E-7	−5.8E-7	1.8E-09
d_c	5.6E-2	1.9E-3[b]			9.1E-7	−1.6E-09
f_i	1.8E-4	1.5E-5[b]				5.4E-11

[a]See Figure 12. All numbers are normalized by the optimum parameter values.
[b]True answer not recovered.

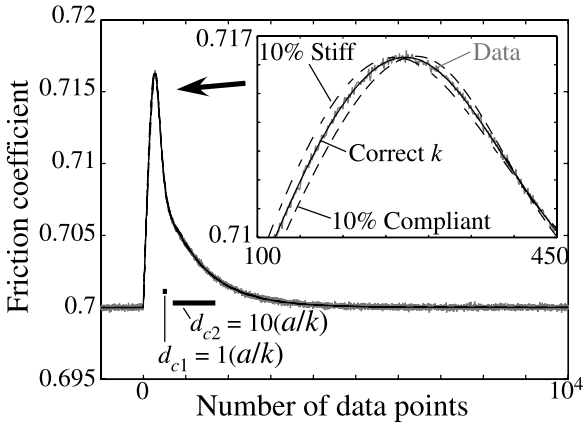

Figure 13. Synthesized experimental data of positive velocity steps by a factor of 10 with two state variables together with the best fit curves with fixed stiffness of the apparatus with $\delta_{c1} = 10$ and $\delta_{c2} = 1$. Two dashed lines represent the best fit curves with 10% higher and lower values of the stiffness of the apparatus, k. Note that the fitting looks excellent graphically although the relative error from the true answer is large (Table 3).

the resulting relative mismatches (deviation of each parameter from its true value), normalized covariance matrix, and twice the standard deviations obtained by the least squares fitting to the same data as for Table 3. The curve fitting is as graphically good as in the case with the correct stiffness in Figure 13 and is not shown here since there is no visible difference between them at the scale of the plot. The relative mismatches for all parameters, including the stiffness, are smaller than 2σ, so that not only the optimum parameter values are successfully determined, but also the length of the error bars. In the inversion of the real friction data of Hanaore fault gouge, we adopted the method described here. We believe that our procedures have general applicability to other testing machines.

5. Constitutive Parameters of Hanaore Fault Gouge

[42] Figure 14a shows the mechanical behavior of the black clayey fault gouge in BAF046. Peak stress at the initial yielding is not significant. The absolute value of friction coefficient is from about 0.43 to 0.62 with displacement hardening throughout the experiments. The overall mechanical behavior is similar to an experiment of 70% quartz and 30% smectite gouge by *Saffer and Marone* [2003] including the rate of strain hardening. Note that the scale of horizontal axis in our work is very different in terms of shear strain from theirs. It should be emphasized that the rate of overall hardening per unit shear strain is in the same order as in the work by *Saffer and Marone* [2003]. We conducted another experiment, BAF045 at identical conditions to BAF046 in terms of the way of water infiltration, the normal stress, and the range of load point velocities. Its overall behavior (the weak appearance of initial peak at the yielding, absolute value of friction, and the rate of strain hardening) is almost identical to BAF 046 and is therefore not shown here.

[43] Figure 15a shows an example of mechanical behavior on a velocity step at low strain rate (BAF046-11, indicated in Figure 14a). The shape of the peak after step is symmetric and different from one observed in an approximately ideal velocity step (Figures 11a and 12a). This suggests that state evolution before shear stress reaches its maximum value is not negligible. In such cases, it is important to treat the stiffness of the apparatus as one of the fitting parameters in order to determine the constitutive parameters, as shown in section 4. The optimum fitting curves themselves are not plotted since it is very difficult to recognize the differences from the data. Instead, the resid-

Table 3. Fitting Results to Positive Velocity Steps With Two State Variables $\delta_{c1} = 1$ and $\delta_{c2} = 10$[a]

			Variance-Covariance Matrix					
	Mismatch	2σ	a	b_1	d_{c1}	b_2	d_{c2}	f_i
Compliant								
a	1.2E-1	4.6E-3[b]	5.4E-6	8.4E-6	−1.3E-5	1.5E-6	−1.2E-6	−2.6E-09
b_1	1.9E-1	7.5E-3[b]		1.4E-5	−1.9E-5	1.5E-6	−9.4E-7	−3.1E-09
d_{c1}	−5.5E-1	1.3E-2[b]			3.9E-5	−5.5E-6	4.9E-6	3.1E-09
b_2	2.3E-2	2.3E-3[b]				1.4E-6	−1.4E-6	9.8E-11
d_{c2}	−1.9E-2	2.9E-3[b]					2.1E-6	3.4E-11
f_i	4.6E-6	1.2E-5[b]						3.5E-11
Correct stiffness								
a	−9.5E-4	2.6E-3	1.6E-6	2.4E-6	−4.9E-6	8.1E-7	−6.1E-7	−1.3E-09
b_1	−2.0E-3	4.3E-3		4.6E-6	−5.3E-6	1.5E-7	1.9E-7	−1.3E-09
d_{c1}	5.8E-3	8.9E-3			2.0E-5	−4.2E-6	3.6E-6	1.6E-09
b_2	−4.9E-4	2.4E-3				1.4E-6	−1.3E-6	−3.0E-11
d_{c2}	2.3E-4	2.6E-3					1.7E-6	8.1E-11
f_i	−5.6E-6	9.1E-6						2.1E-11
Stiff								
a	−7.0E-2	2.7E-3[b]	1.8E-6	2.1E-6	−6.1E-6	1.4E-6	−9.7E-7	−1.8E-09
b_1	−1.1E-1	4.9E-3[b]		6.1E-6	−2.0E-6	−1.6E-6	1.9E-6	−1.3E-09
d_{c1}	2.7E-1	1.1E-2[b]			4.1E-6	−9.5E-6	7.4E-6	2.4E-09
b_2	−3.0E-2	4.0E-3[b]				4.1E-6	−3.5E-6	−1.9E-10
d_{c2}	2.0E-2	3.9E-3[b]					3.9E-6	2.1E-10
f_i	−2.4E-5	1.1E-5[b]						3.4E-11

[a]See Figure 13. All numbers are normalized by the optimum parameter values.
[b]True answer not recovered.

Table 4. Fitting Results to Positive Velocity Steps With Two State Variables $\delta_{c1} = 1$ and $\delta_{c2} = 10$[a]

			Variance-Covariance Matrix						
	Mismatch	2σ	k	a	b_1	d_{c1}	b_2	d_{c2}	f_i
k	−1.6E-3	2.3E-3	1.4E-6	−1.2E-6	−2.0E-6	4.9E-6	−3.6E-7	2.6E-7	−2.1E-10
a	4.1E-4	3.3E-3		2.7E-6	−4.2E-6	−9.2E-6	1.1E-6	−8.4E-7	−1.1E-09
b_1	2.9E-4	5.5E-3			7.6E-6	−1.3E-5	7.0E-7	−2.2E-7	−9.5E-10
d_{c1}	1.3E-4	1.2E-2				3.7E-5	−5.5E-6	4.5E-6	8.9E-11
b_2	−8.1E-5	2.5E-3					1.5E-6	−1.4E-6	2.7E-11
d_{c2}	−7.2E-5	2.6E-3						1.7E-6	3.9E-11
f_i	−5.3E-6	9.1E-6							2.0E-11

[a]See Figure 13. All numbers are normalized by the optimum parameter values. The artificial experimental data is same as for Table 3, but stiffness of the apparatus is treated as one of the fitting parameters.

uals from the best fit cases are plotted in Figure 15b for the slip law (upper) and the aging law (lower). The level of random noise is on the order of 10^{-4} in the friction coefficient in our experimental condition, but the maximum amplitude of the residual is larger almost by an order of magnitude, which appear typically during the peak due to the direct effect. All the fitting results are tabulated in Tables 5 and 6 for the slip law and the aging law, respectively. Figure 14b shows the stiffness of the apparatus determined for each velocity step using the slip law. Error bars indicate twice the standard deviation determined by the numerical fittings. Although each point is determined well, the stiffness value scatters. In many cases, k ranges between 1300 to 2200 m^{-1} with exceptionally large numbers which correspond to long error bars.

[44] Figures 16 and 17 represent determined constitutive parameters in the slip law and the aging law, respectively, plotted as a function of the geometric mean of the slip rates before and after the velocity steps. Several parameters (b_1, and d_{c1} for BAF45-1, -3, and BAF046-1 with the aging law, d_{c1} and d_{c2} for BAF046-3 and a, b_1, and b_2 for BAF046-15 with the slip law) are not plotted in Figures 16 and 17 since they could not be determined precisely; 2σ normalized by the parameter value exceeded 1. Also, the respective values of BAF045-9 could not be determined because of the sampling interval was too long. Otherwise, the error bars are plotted only if they are longer than the symbol size.

[45] The values of $a - \Sigma b$ were successfully determined for all velocity steps (Figures 16a and 17a), and there is no significant difference between the two laws. The length of the error bar for $a - \Sigma b$ was estimated by using the variance-covariance matrices listed in Tables 5 and 6. The $a - \Sigma b$ value changes its signature from negative to positive at a slip rate of around 0.1 μm s^{-1}. *Saffer and Marone* [2003] also observed such a behavior but at a different slip rate (tens of microns per second) for the mixture of quartz and smectites. Because we used much thinner gouge layers than theirs, it is reasonable that we observe this behavior at much lower slip rate if the shear deformation is distributed over a width. This issue is discussed later.

[46] Most of the a values determined are around 0.01 with a few large values typically associated with long error bars (Figure 16b and 17b). This probably implies that the a value is not very sensitive to the slip rate, which is consistent with the interpretation of the direct effect by thermally activated slip process at the solid-solid contacts [e.g., *Nakatani*, 2001; *Rice et al.*, 2001; *Noda*, 2008].

[47] In many (22 out of 25) cases, two state variables are required to fit the experimental data, and all of them yield $b_1 > b_2$ and $d_{c2} > d_{c1}$. For the cases were the experimental behavior is able to fit by one state variable, these b and d_c

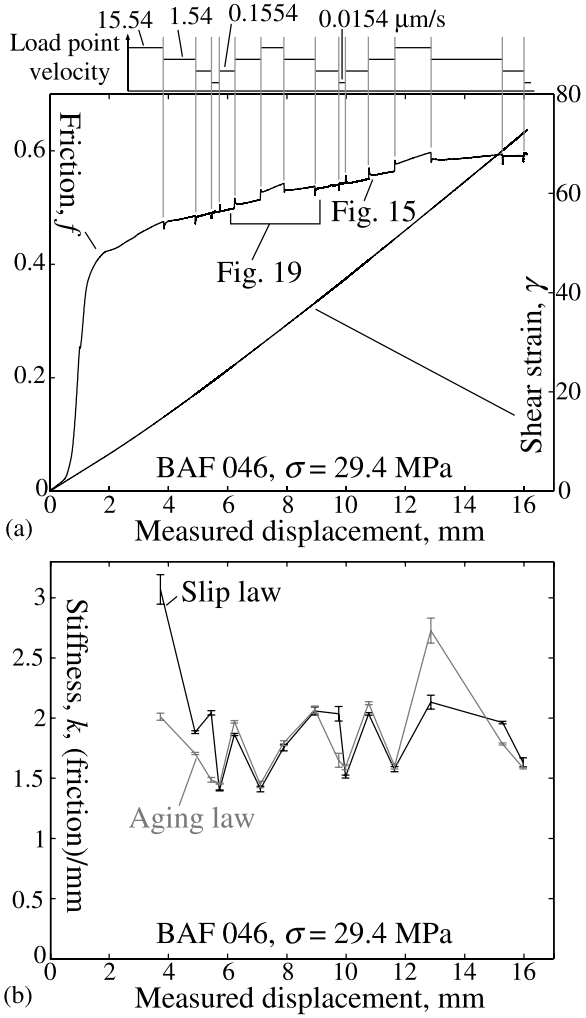

Figure 14. (a) A typical behavior of friction coefficient and integrated shear strain, γ, and (b) determined machine stiffness, k, as a function of measured displacement with the slip law (black) and the aging law (gray). Note that the measured displacement is used to calculate γ so that the true shear strain of the gouge layer is smaller than it especially at the beginning of the loading where the simulated fault is not yet displaced.

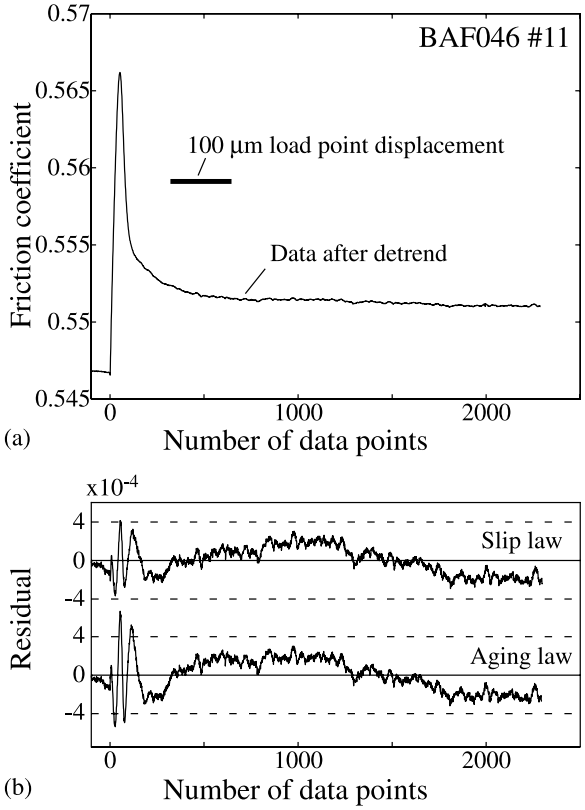

Figure 15. (a) A plot of change in friction coefficient at a velocity step from 0.1554 to 1.54 μm s^{-1} (labeled in Figure 14a) after removing the trend. Rather symmetrical shape (unlike in Figure 1) of the peak implies that state evolution is effective before the peak so that constitutive parameters cannot be determined accurately because of uncertainty in stiffness of the apparatus. (b) The residuals for the best fit curves with (top) the slip law and (bottom) the aging law. The best fit curves themselves are not plotted since they are too close to see the difference.

are plotted as b_1 and d_{c1} in Figures 16c, 17c, 16d, and 17d since the value is close to them. Typically, a negative b_2 value is required to explain the experimental data at relatively high slip rates, an example of which is shown in Figure 18 (BAF046-13). Similar to the a value, b_1 is not remarkably dependent on the slip rate, but b_2 seems to decrease and becomes negative around 1 μm s^{-1}, although the value scatters. In Figure 17d, d_{c1} might increase with increases the slip rate, but the data points off the log-averaged value of d_{c1} have long error bars. In Figure 16d, the value of d_{c1} seems less scattered than in Figure 17d although there is one case which yields extremely short d_{c1}. The d_{c2} seems to increase with slip rate (Figures 16d and 17d) when the negative b_2 appears. It should be emphasized that if a value is 0.01 and k is around 2000 m^{-1}, a/k is about 5 μm, and it is almost always important for us to treat k as one of the fitting parameters in our cases (see section 4).

6. Observation of Microstructure

[48] Figure 19 exhibits typical microstructures after the experiments. The thickness of the gouge layer is about 200 μm. The thin sections were made after specimens are air dried, and during this process the black clayey fault gouge detaches from the host rocks.

[49] Development of Y planes is rarely recognized, but R1 planes are often observed which are typically detached under microscope because of the drying process but have a preferred orientation of platy minerals aligned along them. Between the R1 planes, preferred orientation of platy minerals is observed by forming bands with alternating extinction positions (Figures 18c and 18d). These bands are oriented at very high angle from R1 planes. From the crosscutting relation, these bands are produced prior to the R1 planes.

[50] Previous observations of simulated fault with gouge suggest that the Y plane is developed after the initial peak strength is achieved [*Logan et al.*, 1992]. The poor development of Y planes is consistent with this statement since peak strength at the initial yielding is rarely observed. It is notable that compared to the work by *Saffer and Marone* [2003], the $a - \Sigma b$ values changes its signature at a lower slip rate, suggesting that the actual width of the shear zone developed in the gouge layer is thinner in our study than theirs. The observation supports the argument that strain is not very well localized within the gouge layer by itself, but confined by the gabbro blocks.

[51] Unfortunately, the microstructures observed in the natural outcrop (Figure 4) are not similar to one observed after experiments. For example, the flow-like structure in Figure 4g is similar to one observed in a work by *Mizoguchi and Shimamoto* [2004] after high slip rate experiments which use much greater strain rate and total strain than in this study. The structure in Figure 4i might suggest that this black clayey fault gouge was more indurated before the last event than the experiments in this work, and that deformation mechanism is different. More experimental and microstructural works may be needed to understand how the structure seen on the outcrop is developed.

7. Discussion

[52] Experimental data from velocity step tests have been analyzed using a measured value of the machine stiffness as a fixed parameter, implicitly assumed to be free of error [e.g., *Tullis and Weeks*, 1986; *Marone et al.*, 1990; *Reinen and Weeks*, 1993]. Our modeling results in Figures 11–13 and Tables 1–3 clearly demonstrate that the relative mismatch of the constitutive parameters from the true answer can be larger in some cases than the half length of the error bars (shown as 2σ in Tables 1–3) if the assumed machine stiffness is incorrect. This error is serious when the critical displacement, d_c, is on the same order as the fault displacement from the abrupt change in the loading velocity to the peak/bottom friction for the step increase/decrease in velocity (Tables 1–3). In such cases of small d_c, the effect of an incorrect value of k in shifting the optimum values of the constitutive parameters becomes more important than the effect of superposed random error on the same order as the real experiment of a good quality. Traditional methods of using a fixed stiffness should not be used when d_c is less than at least 100 a/k as shown in the numerical experiments in this work. The stiffness and its fluctuation and/or the fault displacement to peak/bottom friction are not reported in detail in previous work and we cannot comment on the

Table 5. The Results With the Slip Law

			Normalized Variance-Covariance Matrix						
Parameter	Value	Relative 2σ	k	a	b_1	d_{c1}	b_2	d_{c2}	f_i
BAF045-1, Load Point Velocity of 15.54 to 1.54 μm/s									
k (mm^{-1})	2.51E+0	7.7E-2	1.5E-3	−2.7E-4	−5.1E-6	5.8E-5	6.9E-4	−9.7E-5	3.6E-07
a	7.56E-3	2.1E-2		1.1E-4	1.8E-6	−2.4E-5	−2.6E-4	3.8E-5	3.7E-07
b_1	3.74E-3	3.7E-2			3.4E-6	−2.0E-5	−4.0E-4	2.2E-5	9.7E-08
d_{c1} (μm)	1.52E+1	1.0E-2				2.5E-5	1.1E-4	3.7E-5	1.6E-08
b_2	−3.82E-3	5.9E-2					8.6E-4	−1.7E-4	−7.6E-09
d_{c2} (μm)	2.09E+2	2.0E-2						1.0E-4	8.8E-10
f_i	5.18E-1	2.1E-4							1.1E-08
BAF045-2, Load Point Velocity of 1.54 to 15.54 μm/s									
k (mm^{-1})	1.33E+0	2.4E-2	1.4E-4	−4.9E-5	−9.6E-5	2.1E-5	2.1E-4	−1.6E-4	−9.9E-10
a	8.91E-3	1.6E-2		6.4E-5	1.3E-4	−2.1E-5	−2.1E-4	1.9E-4	−2.6E-09
b_1	3.92E-3	3.3E-2			2.8E-4	−3.1E-5	−3.7E-4	6.6E-5	−1.1E-09
d_{c1} (μm)	1.58E+1	4.1E-2				4.2E-4	1.1E-4	6.1E-4	1.2E-10
b_2	−8.80E-4	6.2E-2					9.6E-4	−1.2E-3	1.1E-09
d_{c2} (μm)	4.19E+2	1.6E-1						6.4E-3	−4.8E-10
f_i	5.09E-1	1.9E-5							8.6E-11
BAF045-3, Load Point Velocity of 15.54 to 1.54 μm/s									
k (mm^{-1})	2.75E+0	6.8E-2	1.2E-3	−2.0E-4	−3.0E-4	8.1E-5	4.5E-4	−1.0E-4	5.4E-08
a	8.43E-3	1.8E-2		7.8E-5	1.1E-4	−3.2E-5	−1.7E-4	4.0E-5	4.0E-08
b_1	4.98E-3	2.7E-2			1.8E-4	−2.0E-5	−2.2E-4	1.6E-5	4.6E-09
d_{c1} (μm)	1.66E+1	1.6E-2				6.3E-5	1.2E-4	−8.0E-5	1.1E-09
b_2	−2.49E-3	4.4E-2					4.9E-4	−1.7E-4	9.3E-10
d_{c2} (μm)	2.38E+2	2.7E-2						1.8E-4	−6.8E-10
f_i	5.65E-1	7.2E-5							1.3E-09
BAF045-4, Load Point Velocity of 1.54 to 0.1554 μm/s									
k (mm^{-1})	2.53E+0	3.8E-2	3.7E-4	−7.7E-5	−5.2E-5	1.3E-4	2.2E-4	−8.0E-5	3.7E-07
a	1.10E-2	1.6E-2		6.4E-5	4.3E-5	−6.3E-5	−1.2E-4	4.2E-5	3.7E-07
b_1	8.85E-3	1.4E-2			5.0E-5	−6.3E-6	−6.1E-5	−4.7E-6	5.7E-08
d_{c1} (μm)	1.03E+1	2.6E-2				1.7E-4	2.0E-4	−1.3E-4	9.4E-09
b_2	−3.69E-3	3.5E-2					3.1E-4	−1.4E-4	−4.1E-08
d_{c2} (μm)	7.35E+1	2.3E-2						1.3E-4	−1.2E-08
f_i	5.57E-1	2.4E-4							1.5E-08
BAF045-5, Load Point Velocity of 0.1554 to 0.0154 μm/s									
k (mm^{-1})	1.97E+0	4.0E-3	4.1E-6	−2.7E-6	9.9E-7	−2.8E-5	8.2E-6	1.8E-5	3.2E-09
a	9.26E-3	3.9E-3		3.7E-6	−8.1E-7	3.3E-5	−9.4E-6	−2.1E-5	4.1E-09
b_1	8.88E-3	3.5E-3			3.1E-6	−2.8E-5	5.0E-6	2.2E-5	2.1E-09
d_{c1} (μm)	5.65E+0	4.3E-2				4.5E-4	−1.1E-4	−3.2E-4	−2.7E-09
b_2	1.19E-3	1.1E-2					2.8E-5	7.1E-5	−3.6E-12
d_{c2} (μm)	2.43E+1	3.1E-2						2.4E-4	1.9E-09
f_i	5.48E-1	1.9E-5							9.5E-11
BAF045-6, Load Point Velocity of 0.0154 to 0.1554 μm/s									
k (mm^{-1})	1.43E+0	5.1E-3	6.5E-6	−4.1E-6	−2.6E-6	−6.2E-6	2.0E-5	3.8E-6	−4.3E-10
a	9.03E-3	7.3E-3		1.3E-5	9.2E-6	1.9E-5	−4.3E-5	−1.2E-5	−2.9E-10
b_1	6.07E-3	8.0E-3			1.6E-5	−4.4E-6	−1.6E-5	8.2E-6	−2.4E-10
d_{c1} (μm)	5.67E+0	1.6E-2				6.0E-5	−8.6E-5	−4.8E-5	2.5E-10
b_2	3.30E-3	2.6E-2					1.7E-4	6.1E-5	−2.2E-10
d_{c2} (μm)	3.96E+1	1.4E-2						4.7E-5	−5.1E-11
f_i	5.51E-1	5.8E-6							8.3E-12
BAF045-7, Load Point Velocity of 0.1554 to 1.54 μm/s									
k (mm^{-1})	1.87E+0	9.7E-3	2.3E-5	−1.8E-5	−2.4E-5	−1.7E-5	6.5E-5	1.1E-5	−6.0E-11
a	1.26E-2	1.1E-2		3.0E-5	3.7E-5	3.6E-5	−9.9E-5	−2.3E-5	−3.5E-10
b_1	7.10E-3	1.5E-2			5.8E-5	1.8E-5	−1.1E-4	−5.5E-6	−3.0E-10
d_{c1} (μm)	5.45E+0	2.0E-2				1.0E-4	−1.6E-4	−8.0E-5	5.6E-12
b_2	3.12E-3	3.8E-2					3.7E-4	1.1E-4	3.0E-10
d_{c2} (μm)	4.33E+1	1.8E-2						7.8E-5	1.7E-11
f_i	5.53E-1	6.2E-6							9.6E-12
BAF045-8, Load Point Velocity of 1.54 to 15.54 μm/s									
k (mm^{-1})	1.54E+0	2.8E-2	1.9E-4	−4.5E-5	−8.0E-5	1.1E-5	1.9E-4	−5.1E-5	−1.4E-09
a	1.04E-2	1.5E-2		5.7E-5	1.0E-4	−8.9E-6	−1.6E-4	4.9E-5	−3.3E-09
b_1	5.26E-3	2.8E-2			2.0E-4	−8.3E-6	−2.6E-4	2.1E-5	−1.2E-09
d_{c1} (μm)	1.67E+1	1.5E-2				5.4E-5	4.7E-5	4.1E-5	5.1E-11
b_2	−2.14E-3	5.0E-2					6.3E-4	−2.8E-4	1.2E-09
d_{c2} (μm)	5.99E+2	5.4E-2						7.2E-4	−1.5E-10
f_i	5.66E-1	2.1E-5							1.1E-10

Table 5. (continued)

Parameter	Value	Relative 2σ	Normalized Variance-Covariance Matrix						
			k	a	b_1	d_{c1}	b_2	d_{c2}	f_i
BAF045-9,[a] Load Point Velocity of 15.54 to 155.54 μm/s									
a-Σb	5.4E-3	2.2E-2							
BAF045-10, Load Point Velocity of 155.54 to 15.54 μm/s									
k (mm^{-1})	2.35E+0	1.3E-1	4.3E-3	−7.0E-4	−1.1E-3		1.2E-3		2.6E-7
a	1.19E-2	3.2E-2		2.5E-4	3.7E-4		−4.0E-4		3.1E-7
b_1	7.76E-3	4.8E-2			5.7E-4		−6.1E-4		8.5E-8
d_{c1} (μm)	1.57E+1	5.7E-2					8.0E-4		−2.4E-8
f_i	6.21E-1	2.1E-4							1.1E-8
BAF046-1, Load Point Velocity of 15.54 to 1.54 μm/s									
k (mm^{-1})	3.07E+0	4.0E-2	4.0E-4	−1.9E-5	−3.6E-7	4.9E-5	6.7E-5	−6.0E-5	1.6E-07
a	6.63E-3	7.5E-3		1.4E-5	4.2E-6	−1.3E-5	−1.9E-5	1.6E-5	1.1E-07
b_1	6.92E-3	7.4E-3			1.4E-5	1.9E-5	8.7E-6	−3.4E-5	7.2E-09
d_{c1} (μm)	3.27E+1	1.6E-2				6.7E-5	5.7E-5	−9.3E-5	7.2E-09
b_2	−2.81E-3	1.6E-2					6.5E-5	−7.9E-5	5.3E-09
d_{c2} (μm)	2.44E+2	2.7E-2						1.8E-4	−8.0E-09
f_i	4.71E-1	1.2E-4							3.5E-09
BAF046-2, Load Point Velocity of 1.54 to 0.1554 μm/s									
k (mm^{-1})	1.88E+0	6.3E-3	9.8E-6	−9.7E-6	−7.1E-6	−2.3E-5	2.4E-5	1.2E-5	1.0E-09
a	1.18E-2	7.0E-3		1.2E-5	8.6E-6	3.1E-5	−3.1E-5	−1.7E-5	1.4E-09
b_1	8.39E-3	5.7E-3			8.1E-6	1.4E-5	−1.9E-5	−6.2E-6	7.4E-10
d_{c1} (μm)	5.09E+0	2.0E-2				1.0E-4	−8.5E-5	−6.4E-5	−4.7E-10
b_2	2.34E-3	1.8E-2					7.9E-5	4.9E-5	−1.9E-10
d_{c2} (μm)	2.38E+1	1.3E-2						4.2E-5	1.8E-10
f_i	4.81E-1	1.5E-5							5.5E-11
BAF046-3, Load Point Velocity of 0.1554 to 0.0154 μm/s									
k (mm^{-1})	2.04E+0	9.1E-3	2.0E-5	−9.8E-6	−4.8E-7	6.5E-3	3.0E-5	1.2E-2	3.3E-08
a	7.48E-3	7.4E-3		1.4E-5	2.9E-6	−6.5E-3	−2.9E-5	−1.2E-2	3.5E-08
b_1	7.41E-3	4.5E-3			5.2E-6	2.7E-3	5.3E-7	4.3E-3	1.5E-08
d_{c1} (μm)	5.43E+0	5.5E+0				7.5E+0	2.0E-2	1.3E+1	2.0E-06
b_2	7.95E-5	1.8E-2					7.7E-5	3.5E-3	2.0E-09
d_{c2} (μm)	1.15E+2	9.2E+0						2.1E+1	3.6E-06
f_i	4.88E-1	5.8E-5							8.3E-10
BAF046-4, Load Point Velocity of 0.0154 to 0.1554 μm/s									
k (mm^{-1})	1.40E+0	2.7E-3	1.8E-6	−9.9E-7	1.2E-6	−5.6E-6	6.8E-6	3.2E-6	−2.8E-10
a	7.11E-3	3.5E-3		3.1E-6	−1.9E-6	1.4E-5	−1.3E-5	−8.0E-6	−2.2E-10
b_1	4.66E-3	7.8E-3			1.5E-5	−3.7E-5	2.2E-5	2.8E-5	−2.4E-10
d_{c1} (μm)	6.44E+0	2.2E-2				1.2E-4	−8.8E-5	−8.2E-5	3.3E-10
b_2	2.21E-3	1.7E-2					7.6E-5	5.6E-5	−1.6E-10
d_{c2} (μm)	2.91E+1	1.6E-2						6.5E-5	−1.1E-10
f_i	4.10E-1	4.8E-6							5.7E-12
BAF046-5, Load Point Velocity of 0.1554 to 1.54 μm/s									
k (mm^{-1})	1.86E+0	4.9E-3	6.0E-6	−3.9E-6	−5.7E-6	−3.5E-6	1.6E-5	2.5E-6	−3.3E-11
a	1.06E-2	5.0E-3		6.2E-6	8.6E-6	6.5E-6	−2.2E-5	−4.7E-6	−1.4E-10
b_1	5.52E-3	7.8E-3			1.5E-5	2.5E-6	−2.5E-5	−3.7E-7	−1.1E-10
d_{c1} (μm)	6.29E+0	8.8E-3				1.9E-5	−3.2E-5	−1.6E-5	−2.6E-12
b_2	2.78E-3	1.9E-2					8.9E-5	2.5E-5	1.1E-10
d_{c2} (μm)	5.53E+1	8.5E-3						1.8E-5	8.3E-12
f_i	4.95E-1	4.2E-6							4.3E-12
BAF046-6,Load Point Velocity of 1.54 to 15.54 μm/s									
k (mm^{-1})	1.41E+0	1.6E-2	6.8E-5	−1.8E-5	−3.8E-5	−4.0E-5	7.8E-5	−8.0E-5	−5.3E-10
a	8.96E-3	9.0E-3		2.0E-5	4.2E-5	3.8E-5	−6.4E-5	7.6E-5	−1.3E-09
b_1	3.96E-3	1.9E-2			9.1E-5	1.9E-5	−1.2E-4	4.3E-5	−5.2E-10
d_{c1} (μm)	1.58E+1	7.3E-2				1.3E-3	−2.5E-4	2.3E-3	−1.2E-10
b_2	−2.20E-3	3.4E-2					2.9E-4	−4.9E-4	4.8E-10
d_{c2} (μm)	1.01E+3	1.2E-1						3.9E-3	−2.5E-10
f_i	5.10E-1	1.3E-5							4.3E-11
BAF046-7, Load Point Velocity of 15.54 to 1.54 μm/s									
k (mm^{-1})	1.76E+0	1.6E-2	6.2E-5	−6.8E-5	−1.2E-4	2.0E-7	1.1E-4	−7.7E-6	2.1E-08
a	1.18E-2	1.9E-2		9.4E-5	1.7E-4	−2.0E-7	−1.5E-4	1.2E-5	1.1E-08
b_1	6.49E-3	3.5E-2			3.0E-4	−4.3E-7	−2.7E-4	2.1E-5	2.5E-09
d_{c1} (μm)	5.08E+0	2.5E-3				1.5E-6	1.5E-7	3.3E-6	4.0E-11
b_2	−2.89E-3	3.1E-2					2.4E-4	−2.3E-5	2.4E-09
d_{c2} (μm)	3.99E+2	8.2E-3						1.7E-5	−6.2E-10

Table 5. (continued)

			Normalized Variance-Covariance Matrix						
Parameter	Value	Relative 2σ	k	a	b_1	d_{c1}	b_2	d_{c2}	f_i
f_i	5.39E-1	4.5E-5							5.1E-10
			BAF046-8, Load Point Velocity of 1.54 to 0.1554 μm/s						
k (mm^{-1})	2.06E+0	1.7E-2	6.8E-5	−2.3E-5	−2.9E-5		4.4E-5		7.4E-8
a	1.31E-2	1.2E-2		3.4E-5	3.9E-5		−4.3E-5		1.2E-7
b_1	1.07E-2	1.4E-2			4.6E-5		−5.1E-5		−5.6E-8
d_{c1} (μm)	5.96E+0	1.7E-2					6.8E-5		4.1E-8
f_i	5.34E-1	1.3E-4							4.2E-9
			BAF046-9, Load Point Velocity of 0.1554 to 0.0154 μm/s						
k (mm^{-1})	2.04E+0	2.9E-2	2.2E-4	−1.3E-4	5.5E-6	−2.0E-3	3.7E-4	1.5E-3	1.6E-07
a	8.71E-3	2.9E-2		2.0E-4	2.9E-5	2.4E-3	−4.4E-4	−1.9E-3	2.2E-07
b_1	8.72E-3	1.9E-2			9.2E-5	−8.9E-4	4.5E-5	1.0E-3	1.1E-07
d_{c1} (μm)	4.54E+0	4.3E-1				4.6E-2	−6.8E-3	−4.0E-2	−1.2E-07
b_2	5.86E-4	6.8E-2					1.1E-3	5.6E-3	−2.6E-08
d_{c2} (μm)	2.43E+1	4.0E-1						4.0E-2	1.2E-07
f_i	5.37E-1	1.3E-4							4.5E-09
			BAF046-10, Load Point Velocity of 0.0154 to 0.1554 μm/s						
k (mm^{-1})	1.51E+0	8.0E-3	1.6E-5	9.0E-7	4.1E-6	−9.1E-6	1.7E-5	7.1E-6	−2.6E-09
a	7.53E-3	6.6E-3		1.1E-5	8.0E-6	1.3E-5	−1.9E-5	−1.1E-5	−3.1E-09
b_1	6.45E-3	7.2E-3			1.3E-5	−1.0E-5	−1.3E-6	1.3E-5	−1.5E-09
d_{c1} (μm)	9.07E+0	1.7E-2				7.2E-5	−6.1E-5	−6.9E-5	7.1E-10
b_2	2.18E-3	1.8E-2					7.8E-5	5.5E-5	1.3E-09
d_{c2} (μm)	9.17E+1	2.0E-2						9.7E-5	−2.0E-10
f_i	5.40E-1	1.7E-5							6.8E-11
			BAF046-11, Load Point Velocity of 0.1554 to 1.54 μm/s						
k (mm^{-1})	2.03E+0	5.0E-3	6.2E-6	−3.3E-6	−3.5E-6	−5.0E-6	1.5E-5	3.6E-6	−5.1E-11
a	1.17E-2	4.9E-3		6.0E-6	6.5E-6	8.9E-6	−1.9E-5	−6.5E-6	−2.2E-10
b_1	7.09E-3	6.5E-3			1.0E-5	7.6E-7	−1.5E-5	1.5E-6	−1.4E-10
d_{c1} (μm)	6.67E+0	1.2E-2				3.6E-5	−4.2E-5	−3.0E-5	−8.7E-12
b_2	2.74E-3	1.8E-2					7.7E-5	3.2E-5	1.7E-10
d_{c2} (μm)	5.76E+1	1.2E-2						3.4E-5	1.7E-11
f_i	5.47E-1	5.1E-6							6.6E-12
			BAF046-12, Load Point Velocity of 1.54 to 15.54 μm/s						
k (mm^{-1})	1.58E+0	1.4E-2	4.7E-5	−1.3E-5	−2.3E-5	−5.3E-6	5.2E-5	−1.8E-5	−5.1E-10
a	1.02E-2	8.8E-3		1.9E-5	3.5E-5	6.4E-6	−5.0E-5	2.1E-5	−1.4E-09
b_1	5.26E-3	1.6E-2			6.7E-5	3.4E-6	−8.7E-5	1.4E-5	−6.0E-10
d_{c1} (μm)	1.39E+1	2.0E-2				1.0E-4	−3.5E-5	2.1E-4	−2.4E-11
b_2	−2.84E-3	2.7E-2					1.9E-4	−1.1E-4	5.9E-10
d_{c2} (μm)	1.02E+3	4.5E-2						5.0E-4	−9.6E-11
f_i	5.60E-1	1.4E-5							4.7E-11
			BAF046-13, Load Point Velocity of 15.54 to 1.54 μm/s						
k (mm^{-1})	2.13E+0	2.7E-2	1.9E-4	−9.0E-5	−1.6E-4	4.2E-6	1.6E-4	−6.2E-6	8.1E-08
a	1.10E-2	1.7E-2		7.1E-5	1.2E-4	−3.5E-6	−1.2E-4	5.2E-6	7.1E-08
b_1	6.10E-3	3.0E-2			2.2E-4	−5.5E-6	−2.2E-4	7.7E-6	2.6E-08
d_{c1} (μm)	8.88E+0	2.3E-3				1.3E-6	8.5E-6	−1.5E-6	8.8E-10
b_2	−4.22E-3	3.1E-2					2.4E-4	−1.3E-5	−5.6E-09
d_{c2} (μm)	4.06E+2	4.7E-3						5.5E-6	−5.9E-11
f_i	5.94E-1	9.9E-5							2.5E-09
			BAF046-14, Load Point Velocity of 1.54 to 0.1554 μm/s						
k (mm^{-1})	1.96E+0	5.1E-3	6.5E-6	−8.6E-6	−5.9E-6	−3.1E-5	2.0E-5	1.6E-5	7.8E-10
a	1.69E-2	7.8E-3		1.5E-5	1.0E-5	5.8E-5	−3.4E-5	−3.0E-5	2.1E-09
b_1	1.34E-2	5.6E-3			7.9E-6	2.9E-5	−2.1E-5	−1.3E-5	1.4E-09
d_{c1} (μm)	4.54E+0	3.3E-2				2.7E-4	−1.4E-4	−1.5E-4	−2.3E-10
b_2	2.13E-3	1.8E-2					7.8E-5	7.3E-5	−1.1E-09
d_{c2} (μm)	2.16E+1	1.9E-2						9.0E-5	5.5E-11
f_i	5.91E-1	1.6E-5							6.6E-11
			BAF046-15, Load Point Velocity of 0.1554 to 0.0154 μm/s						
k (mm^{-1})	1.63E+0	2.3E-2	1.3E-4	−1.2E-2	−1.2E-2	−5.7E-5	1.2E-2	7.2E-5	2.2E-09
a	1.08E-1	2.1E+0		1.1E+0	1.1E+0	5.2E-3	−1.1E+0	−6.5E-3	−7.8E-08
b_1	1.04E-1	2.1E+0			1.2E+0	5.5E-3	−1.2E+0	−6.8E-3	−8.1E-08
d_{c1} (μm)	1.15E-1	1.1E-2				2.9E-5	−5.5E-3	−3.5E-5	−4.0E-10

Table 5. (continued)

			Normalized Variance-Covariance Matrix						
Parameter	Value	Relative 2σ	k	a	b_1	d_{c1}	b_2	d_{c2}	f_i
b_2	6.56E-3	2.2E+0					1.2E+0	6.9E-3	8.5E-08
d_{c2} (μm)	8.00E+0	1.3E-2						4.3E-5	7.1E-10
f_i	5.89E-1	1.2E-5							3.9E-11

[a]Only $a - \Sigma b$ was determined. The state evolution equation does not matter.

validity of previous measurements of the constitutive parameters.

[53] The alternative and simple method we propose in this paper is to treat the machine stiffness as an unknown parameter in exactly the same manner as the frictional constitutive parameters are treated. The results in Table 4 show that all the constitutive parameters are recovered within the estimated errors. We emphasize that there is no need to determine the stiffness of the apparatus precisely prior to experiments in this revised method. The only assumption we made is that the apparatus is linearly elastic in each velocity step portion of the experiment, but not in the entire experiments like in the work by *Blanpied et al.* [1998]. We consider that this assumption is reasonable in view of the systematic loading behavior of our machine (Figure 9) and small amount of change in the friction coefficient relative to its absolute value. Note that time-dependent inelastic deformation of the apparatus probably becomes important in experiments with extremely low loading velocities. In such cases, the assumption we take is no longer valid and the precise determination of the constitutive parameters requires us to solve the coupling of the frictional surface and the elastic-plastic apparatus or the determined fault constitutive parameters are affected by the plastic deformation of the apparatus.

[54] *Reinen and Weeks* [1993] discussed the effect of the stiffness value as a fixed parameter since they can control it when using a high-speed servo-control system. They do not treat the machine stiffness, k as a fitting parameter, and the error in it is not reported in their variance-covariance matrix. *Blanpied et al.* [1998] determined k for each velocity step using the rate of change in the friction coefficient just after the velocity step and reported that it varied for one velocity step to another. We think this method is reasonable although they cannot determine the error bar in it. It is true that the machine stiffness affects the initial slope in friction coefficient toward the peak friction due to the direct effect as shown in equation (9), but it also affects the overall frictional behavior especially when one of the d_c is very small. So, we think that it is more reasonable to determine k using entire data set, not only just after the step.

[55] Our biaxial apparatus was designed for high-temperature friction experiments and its stiffness property is not ideal; the machine is compliant and the stiffness varies considerably. This is because the specimen assembly in the furnace consists of several elements such as ceramic pistons, temperature-resistant stainless-steel spacers, metal pistons and rock specimens [see *Kawamoto and Shimamoto*, 1997, 1998]. We expect that most other similar machines are superior with regards to the stiffness fluctuation. After investigating the mechanical property of the apparatus, we conclude that treating the machine stiffness as an unknown parameter in the analysis of specimen-apparatus interaction for the velocity step test is the best way to experimentally determine the fault constitutive parameters at the present time. Of course, specimen-apparatus interaction does not have to be analyzed for the estimate of constitutive parameters if an ideal step change in slip rate along fault is attained in experiments by monitoring the fault displacement and controlling it via servo-control.

[56] We reemphasize that a big advantage of biaxial machines [e.g., *Hoskins et al.*, 1968; *Dieterich*, 1979, 1981; *Marone*, 1998; *Saffer and Marone*, 2003] (our machine) is their high sensitivity of friction measurements because the loading column and the specimen assembly are free from O-rings and jackets. Fault constitutive properties are so subtle that we are not sure how much errors in the estimate of constitutive parameters are induced, for instance, by jacket strength and friction between the end of a precut specimen and piston in triaxial experiments or by O-ring or any other friction in rotary shear experiments. Despite the success of fault constitutive laws, we are currently faced with describing the complex constitutive behavior of clayey fault gouges whose constitutive parameters change substantially with ambient conditions and slip rate [e.g., *Logan and Rauenzahn*, 1987; *Morrow et al.*, 2000; *Bos et al.*, 2000; *Niemeijer and Spiers*, 2006]. This could be due to partial operation of plastic deformation such as basal plane slip in sheet silicate minerals. Under deeper conditions and at very slow slip rates under fluid-rich environments, plastic deformation in granular minerals and solution/precipitation creep may enter into the processes [e.g., *Shimamoto*, 1986; *Bos and Spiers*, 2002]. Thus, accurate measurements of constitutive parameters still remain to be experimental challenges.

[57] Figures 16 and 17 show that the data points scatter much more widely than the error bars determined by least squares fitting for respective velocity steps so that the overall error is determined by the experimental reproducibility. From Tables 1–3, the relative mismatch is at most on the order of 10%, and not by orders of magnitude. Thus, the new method we adopted in this work might not make a critical difference in previously reported data, although the treatment of the machine stiffness as one of the fitting parameter is essential to estimate mathematically correct optimum parameter values and errors. Comparing the two constitutive laws (the slip law and the aging law), the slip law seems to do a better job since the data points seems so scatter widely in Figure 17 than in Figure 16.

[58] Figure 20 is a magnified plot of the change in friction coefficient (BAF046-5, -6, and -7, indicated in Figure 14a). Apparently, the slope of strain hardening is steeper at high slip rate (15.54 μm s^{-1}) than at the lower slip rates, which can be recognized in Figure 14a as well. It is notable that

Table 6. The Results With the Aging Law

			Normalized Variance-Covariance Matrix						
Parameter	Value	Relative 2σ	k	a	b_1	d_{c1}	b_2	d_{c2}	f_i
BAF045-1, Load Point Velocity of 15.54 to 1.54 μm/s									
k (mm^{-1})	2.44E+0	5.2E-2	6.8E-4	−3.9E-5	5.0E-3	5.0E-3	8.7E-4	−7.6E-4	2.8E-07
a	7.50E-3	1.1E-2		3.0E-5	−2.1E-3	−2.1E-3	−3.7E-4	3.2E-4	2.6E-07
b_1	3.15E-2	1.5E+0			5.6E-1	5.6E-1	9.2E-2	−8.9E-2	−1.0E-06
d_{c1} (μm)	9.51E+1	1.5E+0				5.6E-1	9.2E-2	−8.9E-2	−1.0E-06
b_2	−3.15E-2	2.5E-1					1.5E-2	1.5E-2	−1.9E-07
d_{c2} (μm)	1.31E+2	2.4E-1						1.4E-2	1.6E-07
f_i	5.19E-1	1.8E-4							8.1E-09
BAF045-2, Load Point Velocity of 1.54 to 15.54 μm/s									
k (mm^{-1})	1.35E+0	2.5E-2	1.5E-4	−5.2E-5	−1.2E-4	2.4E-5	1.8E-4	−4.8E-5	−1.0E-09
a	8.69E-3	1.5E-2		5.9E-5	1.3E-4	−2.2E-5	−1.6E-4	5.3E-5	−2.6E-09
b_1	3.63E-3	3.6E-2			3.2E-4	−1.6E-5	−3.3E-4	6.2E-6	−1.1E-09
d_{c1} (μm)	9.64E+0	3.7E-2				3.4E-4	1.3E-4	1.1E-4	9.5E-11
b_2	−7.26E-4	4.8E-2					5.8E-4	−3.2E-4	6.5E-10
d_{c2} (μm)	1.98E+2	8.8E-2						1.9E-3	−1.0E-10
f_i	5.09E-1	1.8E-5							8.5E-11
BAF045-3, Load Point Velocity of 15.54 to 1.54 μm/s									
k (mm^{-1})	2.78E+0	5.2E-2	6.7E-4	−4.0E-5	3.8E-3	4.2E-3	7.3E-4	−6.5E-4	4.2E-08
a	8.15E-3	9.5E-3		2.2E-5	−1.5E-3	−1.7E-3	−2.9E-4	2.6E-4	3.1E-08
b_1	2.82E-2	1.1E+0			3.1E-1	3.4E-1	5.6E-2	−5.5E-2	−5.0E-08
d_{c1} (μm)	9.53E+1	1.2E+0				3.7E-1	6.1E-2	−6.0E-2	−5.5E-08
b_2	−2.59E-2	2.0E-1					1.0E-2	−9.8E-3	−1.0E-08
d_{c2} (μm)	1.34E+2	2.0E-1						9.7E-3	8.2E-09
f_i	5.65E-1	6.3E-5							9.9E-10
BAF045-4, Load Point Velocity of 1.54 to 0.1554 μm/s									
k (mm^{-1})	2.43E+0	2.9E-2	2.2E-4	−7.1E-6	5.8E-4	7.5E-4	2.2E-4	−1.8E-4	4.2E-07
a	1.16E-2	1.1E-2		3.3E-5	−3.8E-4	−5.1E-4	−1.5E-4	1.2E-4	4.0E-07
b_1	2.62E-2	2.5E-1			1.6E-2	2.1E-2	5.6E-3	−5.5E-3	−3.2E-07
d_{c1} (μm)	3.07E+1	3.3E-1				2.7E-2	7.3E-3	−7.0E-3	−4.5E-07
b_2	−2.05E-2	8.9E-2					2.0E-3	−1.9E-3	−1.8E-07
d_{c2} (μm)	5.48E+1	8.6E-2						1.8E-3	8.8E-08
f_i	5.57E-1	2.5E-4							1.6E-08
BAF045-5, Load Point Velocity of 0.1554 to 0.0154 μm/s									
k (mm^{-1})	1.74E+0	3.3E-3	2.7E-6	−3.2E-6	−1.5E-6	−5.4E-6	1.3E-5	3.2E-6	3.2E-09
a	1.10E-2	5.5E-3		7.5E-6	2.9E-6	4.3E-5	−2.7E-5	−8.5E-6	3.1E-09
b_1	7.28E-3	6.1E-3			9.2E-6	−7.8E-6	−1.5E-6	8.4E-6	3.5E-09
d_{c1} (μm)	4.18E+0	1.3E-2				4.4E-5	−6.3E-5	−3.3E-5	−2.2E-09
b_2	4.50E-3	2.1E-2					1.1E-4	4.3E-5	2.5E-09
d_{c2} (μm)	2.35E+1	1.1E-2						2.8E-5	5.5E-10
f_i	5.48E-1	1.8E-5							8.1E-11
BAF045-6, Load Point Velocity of 0.0154 to 0.1554 μm/s									
k (mm^{-1})	1.50E+0	5.1E-3	6.5E-6	−1.5E-6	−3.4E-7	−4.7E-6	8.8E-6	3.0E-6	−3.8E-10
a	8.22E-3	4.7E-3		5.6E-6	4.4E-6	8.3E-6	−1.1E-5	−5.2E-6	−3.4E-10
b_1	6.44E-3	5.6E-3			7.9E-6	−6.8E-6	−3.2E-6	6.2E-6	−1.7E-10
d_{c1} (μm)	4.99E+0	1.5E-2				5.3E-5	−3.2E-5	−3.8E-5	1.6E-10
b_2	2.12E-3	1.2E-2					3.4E-5	2.1E-5	1.4E-11
d_{c2} (μm)	2.80E+1	1.3E-2						5.0E-5	−4.0E-11
f_i	5.51E-1	5.8E-6							8.3E-12
BAF045-7, Load Point Velocity of 0.1554 to 1.54 μm/s									
k (mm^{-1})	1.98E+0	9.6E-3	2.3E-5	−9.9E-6	−1.2E-5	−1.3E-5	3.1E-5	7.7E-6	−8.3E-11
a	1.15E-2	7.1E-3		1.3E-5	1.6E-5	1.6E-5	−3.1E-5	−1.0E-5	−3.4E-10
b_1	6.92E-3	1.0E-2			2.6E-5	−3.7E-7	−3.1E-5	3.1E-6	−2.0E-10
d_{c1} (μm)	4.88E+0	1.9E-2				8.7E-5	−6.5E-5	−6.2E-5	−5.4E-12
b_2	2.17E-3	2.0E-2					9.6E-5	4.2E-5	1.5E-10
d_{c2} (μm)	3.05E+1	1.6E-2						6.4E-5	1.3E-11
f_i	5.53E-1	6.5E-6							1.1E-11
BAF045-8, Load Point Velocity of 1.54 to 15.54 μm/s									
k (mm^{-1})	1.55E+0	2.6E-2	1.7E-4	−4.7E-5	−9.5E-5	8.5E-6	1.5E-4	−1.2E-5	−1.0E-09
a	1.02E-2	1.4E-2		5.0E-5	1.0E-4	−6.7E-6	−1.2E-4	1.2E-5	−2.7E-09
b_1	4.96E-3	2.9E-2			2.0E-4	−4.3E-6	−2.2E-4	3.1E-6	−1.0E-09
d_{c1} (μm)	9.57E+0	1.2E-2				3.8E-5	3.3E-5	1.1E-6	2.1E-11
b_2	−1.82E-3	3.9E-2					3.8E-4	−6.3E-5	6.5E-10
d_{c2} (μm)	2.90E+2	2.7E-2						1.9E-4	−2.1E-11
f_i	5.66E-1	1.9E-5							9.1E-11

Table 6. (continued)

Parameter	Value	Relative 2σ	Normalized Variance-Covariance Matrix						
			k	a	b_1	d_{c1}	b_2	d_{c2}	f_i
BAF045-9,[a] Load Point Velocity of 15.54 to 155.54 μm/s									
a-Σb	5.40E-03	2.2E-2							
BAF045-10, Load Point Velocity of 155.54 to 15.54 μm/s									
k (mm^{-1})	1.97E+0	8.6E-2	1.8E-3	−2.4E-4	−3.6E-4		6.9E-4		2.8E-7
a	1.32E-2	2.6E-2		1.7E-4	2.3E-4		−3.4E-4		3.0E-7
b_1	9.07E-3	3.6E-2			3.3E-4		−4.8E-4		1.1E-7
d_{c1} (μm)	2.18E+1	6.0E-2					9.0E-4		−7.4E-8
f_i	6.21E-1	2.1E-4							1.1E-8
BAF046-1, Load Point Velocity of 15.54 to 1.54 μm/s									
k (mm^{-1})	2.01E+0	1.5E-2	5.6E-5	3.8E-7	1.6E-3	1.8E-3	1.5E-4	−1.5E-4	4.6E-08
a	7.67E-3	4.0E-3		4.0E-6	−9.1E-4	−9.9E-4	−8.4E-5	8.6E-5	3.5E-08
b_1	6.27E-2	1.9E+0			8.8E-1	9.6E-1	7.9E-2	−8.5E-2	−3.3E-07
d_{c1} (μm)	1.12E+2	2.1E+0				1.1E+0	8.7E-2	−9.3E-2	−3.7E-07
b_2	−5.75E-2	1.7E-1					7.1E-3	−7.7E-3	−3.3E-08
d_{c2} (μm)	1.34E+2	1.8E-1						8.2E-3	3.0E-08
f_i	4.71E-1	6.9E-5							1.2E-09
BAF046-2, Load Point Velocity of 1.54 to 0.1554 μm/s									
k (mm^{-1})	1.71E+0	5.5E-3	7.6E-6	−1.5E-5	−2.3E-5	−5.1E-6	3.9E-5	3.3E-6	1.1E-09
a	1.46E-2	1.3E-2		4.0E-5	5.7E-5	1.7E-5	−1.0E-4	−1.2E-5	1.4E-09
b_1	8.72E-3	1.8E-2			8.4E-5	2.0E-5	−1.4E-4	−1.2E-5	1.3E-09
d_{c1} (μm)	3.33E+0	8.0E-3				1.6E-5	−5.2E-5	−1.3E-5	−4.1E-10
b_2	4.82E-3	3.3E-2					2.7E-4	3.7E-5	3.0E-11
d_{c2} (μm)	2.86E+1	7.0E-3						1.2E-5	2.1E-11
f_i	4.81E-1	1.5E-5							5.3E-11
BAF046-3, Load Point Velocity of 0.1554 to 0.0154 μm/s									
k (mm^{-1})	1.49E+0	1.4E-2	4.8E-5	−1.6E-3	−1.8E-3	1.2E-5	1.8E-3	−6.0E-6	3.2E-08
a	4.14E-2	4.8E-1		5.8E-2	6.6E-2	−1.5E-4	−6.7E-2	−9.9E-6	−4.1E-07
b_1	3.63E-2	5.5E-1			7.5E-2	−1.8E-4	−7.6E-2	−7.7E-6	−4.8E-07
d_{c1} (μm)	2.34E-1	8.5E-3				1.8E-5	1.5E-4	−1.8E-5	8.4E-09
b_2	5.05E-3	5.6E-1					7.8E-2	3.8E-5	5.1E-07
d_{c2} (μm)	1.17E+1	9.3E-3						2.2E-5	−1.1E-08
f_i	4.88E-1	4.4E-5							4.8E-10
BAF046-4, Load Point Velocity of 0.0154 to 0.1554 μm/s									
k (mm^{-1})	1.45E+0	2.9E-3	2.1E-6	−5.0E-7	3.4E-7	−3.8E-6	3.1E-6	2.2E-6	−2.9E-10
a	6.67E-3	2.6E-3		1.7E-6	6.3E-7	5.9E-6	−3.8E-6	−3.4E-6	−2.7E-10
b_1	5.12E-3	4.0E-3			4.0E-6	−1.2E-5	2.2E-6	9.2E-6	−1.4E-10
d_{c1} (μm)	4.97E+0	1.7E-2				7.5E-5	−2.7E-5	−5.0E-5	2.2E-10
b_2	1.31E-3	7.6E-3					1.4E-5	1.7E-5	−6.9E-12
d_{c2} (μm)	2.07E+1	1.3E-2						4.5E-5	−7.9E-11
f_i	4.90E-1	5.1E-6							6.5E-12
BAF046-5, Load Point Velocity of 0.1554 to 1.54 μm/s									
k (mm^{-1})	1.97E+0	5.3E-3	6.9E-6	−2.6E-6	−3.8E-6	−2.5E-6	9.1E-6	1.7E-6	−5.0E-11
a	9.76E-3	3.7E-3		3.4E-6	5.0E-6	3.1E-6	−8.6E-6	−2.1E-6	−1.6E-10
b_1	5.40E-3	6.1E-3			9.3E-6	−7.7E-7	−9.8E-6	1.2E-6	−8.2E-11
d_{c1} (μm)	5.37E+0	8.1E-3				1.7E-5	−1.5E-5	−1.2E-5	−3.1E-12
b_2	2.08E-3	1.1E-2					2.9E-5	1.0E-5	6.2E-11
d_{c2} (μm)	3.81E+1	7.6E-3						1.5E-5	6.0E-12
f_i	4.95E-1	4.6E-6							5.3E-12
BAF046-6, Load Point Velocity of 1.54 to 15.54 μm/s									
k (mm^{-1})	1.45E+0	1.8E-2	8.2E-5	−2.2E-5	−5.0E-5	−8.0E-6	7.5E-5	−2.6E-5	−6.0E-10
a	8.70E-3	9.0E-3		2.0E-5	4.7E-5	7.3E-6	−5.4E-5	2.2E-5	−1.4E-09
b_1	3.65E-3	2.1E-2			1.1E-4	−8.7E-7	−1.2E-4	3.3E-6	−5.4E-10
d_{c1} (μm)	9.80E+0	3.8E-2				3.6E-4	−4.6E-5	6.0E-4	−1.1E-11
b_2	−1.51E-3	2.8E-2					2.0E-4	−1.4E-4	3.1E-10
d_{c2} (μm)	3.16E+2	6.7E-2						1.1E-3	−4.9E-11
f_i	5.10E-1	1.4E-5							4.8E-11
BAF046-7, Load Point Velocity of 15.54 to 1.54 μm/s									
k (mm^{-1})	1.79E+0	1.1E-2	3.0E-5	−2.5E-5	−4.5E-5	−1.9E-6	5.4E-5	−1.2E-5	1.5E-08
a	1.16E-2	1.1E-2		3.2E-5	5.5E-5	3.1E-6	−6.9E-5	1.8E-5	9.6E-09
b_1	6.37E-3	2.0E-2			9.8E-5	4.8E-6	−1.2E-4	2.8E-5	3.4E-09
d_{c1} (μm)	7.74E+0	4.1E-3				4.2E-6	−9.1E-6	1.4E-5	−1.7E-10
b_2	−3.96E-3	2.5E-2					1.6E-4	−5.0E-5	5.0E-10
d_{c2} (μm)	1.50E+3	1.5E-2						5.4E-5	−1.0E-09

Table 6. (continued)

			Normalized Variance-Covariance Matrix						
Parameter	Value	Relative 2σ	k	a	b_1	d_{c1}	b_2	d_{c2}	f_i
f_i	5.39E-1	3.9E-5							3.9E-10
			BAF046-8, Load Point Velocity of 1.54 to 0.1554 μm/s						
k (mm^{-1})	2.07E+0	1.5E-2	5.5E-5	−9.0E-6	−1.3E-5		3.3E-5		9.6E-8
a	1.37E-2	9.7E-3		2.3E-5	2.6E-5		−3.5E-5		1.3E-7
b_1	1.13E-2	1.1E-2			2.9E-5		−4.0E-5		6.8E-8
d_{c1} (μm)	8.42E+0	1.7E-2					7.3E-5		−6.3E-8
f_i	5.34E-1	1.4E-4							4.6E-9
			BAF046-9, Load Point Velocity of 0.1554 to 0.0154 μm/s						
k (mm^{-1})	1.65E+0	3.5E-2	3.1E-4	−1.3E-3	−1.8E-3	−1.5E-4	2.5E-3	8.7E-5	1.9E-07
a	1.51E-2	1.8E-1		7.7E-3	1.0E-2	1.3E-3	−1.4E-2	−9.1E-4	4.3E-08
b_1	1.08E-2	2.3E-1			1.3E-2	1.6E-3	−1.9E-2	−1.0E-3	−1.2E-08
d_{c1} (μm)	1.29E+0	5.0E-2				6.4E-4	−2.9E-3	−5.7E-4	−4.0E-08
b_2	4.83E-3	3.3E-1					2.8E-2	2.1E-3	3.7E-07
d_{c2} (μm)	1.49E+1	5.0E-2						6.1E-4	−2.9E-08
f_i	5.37E-1	1.3E-4							4.2E-09
			BAF046-10, Load Point Velocity of 0.0154 to 0.1554 μm/s						
k (mm^{-1})	1.59E+0	1.2E-2	3.5E-5	1.2E-6	4.0E-6	−1.0E-5	1.9E-5	6.8E-6	−3.3E-09
a	7.19E-3	7.0E-3		1.2E-5	1.1E-5	7.4E-6	−1.4E-5	−5.7E-6	−4.0E-09
b_1	6.52E-3	7.6E-3			1.5E-5	−7.9E-6	−6.8E-6	7.7E-6	−1.3E-09
d_{c1} (μm)	5.91E+0	1.5E-2				5.9E-5	−3.2E-5	−4.7E-5	4.7E-10
b_2	1.76E-3	1.3E-2					4.2E-5	2.5E-5	1.3E-09
d_{c2} (μm)	5.52E+1	1.7E-2						7.3E-5	−3.1E-11
f_i	5.40E-1	1.9E-5							8.8E-11
			BAF046-11, Load Point Velocity of 0.1554 to 1.54 μm/s						
k (mm^{-1})	2.12E+0	5.9E-3	8.7E-6	−3.2E-6	−3.8E-6	−4.1E-6	1.1E-5	2.9E-6	−8.0E-11
a	1.10E-2	4.5E-3		5.0E-6	6.3E-6	5.3E-6	−1.1E-5	−3.6E-6	−2.9E-10
b_1	6.96E-3	6.4E-3			1.0E-5	−1.1E-6	−1.1E-5	1.8E-6	−1.4E-10
d_{c1} (μm)	5.11E+0	1.1E-2				3.1E-5	−2.2E-5	−2.4E-5	−6.4E-12
b_2	2.11E-3	1.2E-2					3.5E-5	1.6E-5	1.2E-10
d_{c2} (μm)	3.74E+1	1.1E-2						2.9E-5	1.2E-11
f_i	5.47E-1	6.0E-6							9.0E-12
			BAF046-12, Load Point Velocity of 1.54 to 15.54 μm/s						
k (mm^{-1})	1.60E+0	1.4E-2	4.9E-5	−1.5E-5	−2.9E-5	8.4E-8	4.7E-5	−4.9E-6	−4.7E-10
a	9.98E-3	8.6E-3		1.9E-5	3.7E-5	1.5E-7	−4.1E-5	5.5E-6	−1.3E-99
b_1	4.95E-3	1.7E-2			7.3E-5	−4.1E-7	−7.9E-5	1.9E-6	−5.6E-10
d_{c1} (μm)	8.39E+0	1.0E-2				2.7E-5	−1.1E-6	4.5E-5	1.2E-12
b_2	−2.18E-3	2.3E-2					1.3E-4	−2.8E-5	−3.7E-10
d_{c2} (μm)	3.78E+2	2.2E-2						1.3E-4	1.5E-11
f_i	5.60E-1	1.3E-5							4.4E-11
			BAF046-13, Load Point Velocity of 15.54 to 1.54 μm/s						
k (mm^{-1})	2.73E+0	3.8E-2	3.7E-4	−3.4E-5	−3.4E-5	2.7E-5	1.5E-4	−3.5E-5	2.5E-07
a	9.03E-3	1.0E-2		2.7E-5	1.9E-5	−1.3E-5	−7.2E-5	1.7E-5	1.7E-07
b_1	5.84E-3	1.3E-2			4.4E-5	1.2E-5	−1.2E-5	−2.4E-5	1.5E-08
d_{c1} (μm)	4.34E+1	1.0E-2				2.7E-5	8.6E-5	−4.2E-5	−2.5E-10
b_2	−6.04E-3	3.8E-2					3.6E-4	−1.2E-4	−1.3E-08
d_{c2} (μm)	5.95E+2	1.8E-2						7.7E-5	1.4E-09
f_i	5.94E-1	1.5E-4							5.6E-09
			BAF046-14, Load Point Velocity of 1.54 to 0.1554 μm/s						
k (mm^{-1})	1.78E+0	4.7E-3	5.4E-6	−1.6E-5	−2.0E-5	−4.6E-6	3.1E-5	2.7E-6	9.6E-10
a	2.39E-2	1.5E-2		5.8E-5	7.4E-5	2.2E-5	−1.1E-4	−1.4E-5	2.1E-09
b_1	1.73E-2	1.9E-2			9.4E-5	2.5E-5	−1.4E-4	−1.5E-5	2.2E-09
d_{c1} (μm)	2.49E+0	8.1E-3				1.7E-5	−4.7E-5	−1.3E-5	−7.5E-10
b_2	5.20E-3	3.0E-2					2.2E-4	3.1E-5	−5.5E-10
d_{c2} (μm)	2.55E+1	7.0E-3						1.2E-5	6.3E-11
f_i	5.91E-1	1.6E-5							6.2E-11
			BAF046-15, Load Point Velocity of 0.1554 to 0.0154 μm/s						
k (mm^{-1})	1.58E+0	3.5E-3	3.0E-6	−8.3E-5	−9.3E-5	2.1E-7	9.8E-5	8.4E-7	7.7E-10
a	4.43E-2	1.0E-1		2.7E-3	3.0E-3	9.9E-6	−3.2E-3	−4.8E-5	−3.4E-09
b_1	3.92E-2	1.2E-1			3.4E-3	1.1E-5	−3.6E-3	−5.4E-5	−3.9E-09
d_{c1} (μm)	2.78E-1	2.1E-3				1.2E-6	−1.3E-5	−2.0E-6	2.1E-11
b_2	6.87E-3	1.2E-1					3.8E-3	6.0E-5	5.6E-09

Table 6. (continued)

			Normalized Variance-Covariance Matrix						
Parameter	Value	Relative 2σ	k	a	b_1	d_{c1}	b_2	d_{c2}	f_i
d_{c2} (μm)	1.53E+1	4.5E-3						5.1E-6	−1.4E-10
f_i	5.89E-1	8.5E-6							1.8E-11

[a]Only a − Σb was determined. The state evolution equation does not matter.

typically in the following negative velocity steps evolution of friction coefficient shows a behavior with a negative b_2 value; a peak followed by rapid decay and another slow decay in the opposite direction. This implies that the apparently steeper displacement strengthening is due to evolution of second state variable with negative b_2 and long d_{c2}, and indeed, they are required in the numerical fittings. The upward convexity observed at the high slip rate (15.54 μm s^{-1}) might include some contribution from the overall hardening behavior which is convex upward, but it must have only a minor effect since the rate of hardening is apparently too high at 15.54 μm s^{-1}, and it cannot explain the second decay in the following velocity step.

[59] Dilatation of the gouge layer and following fluid transportation might affect measured friction coefficient

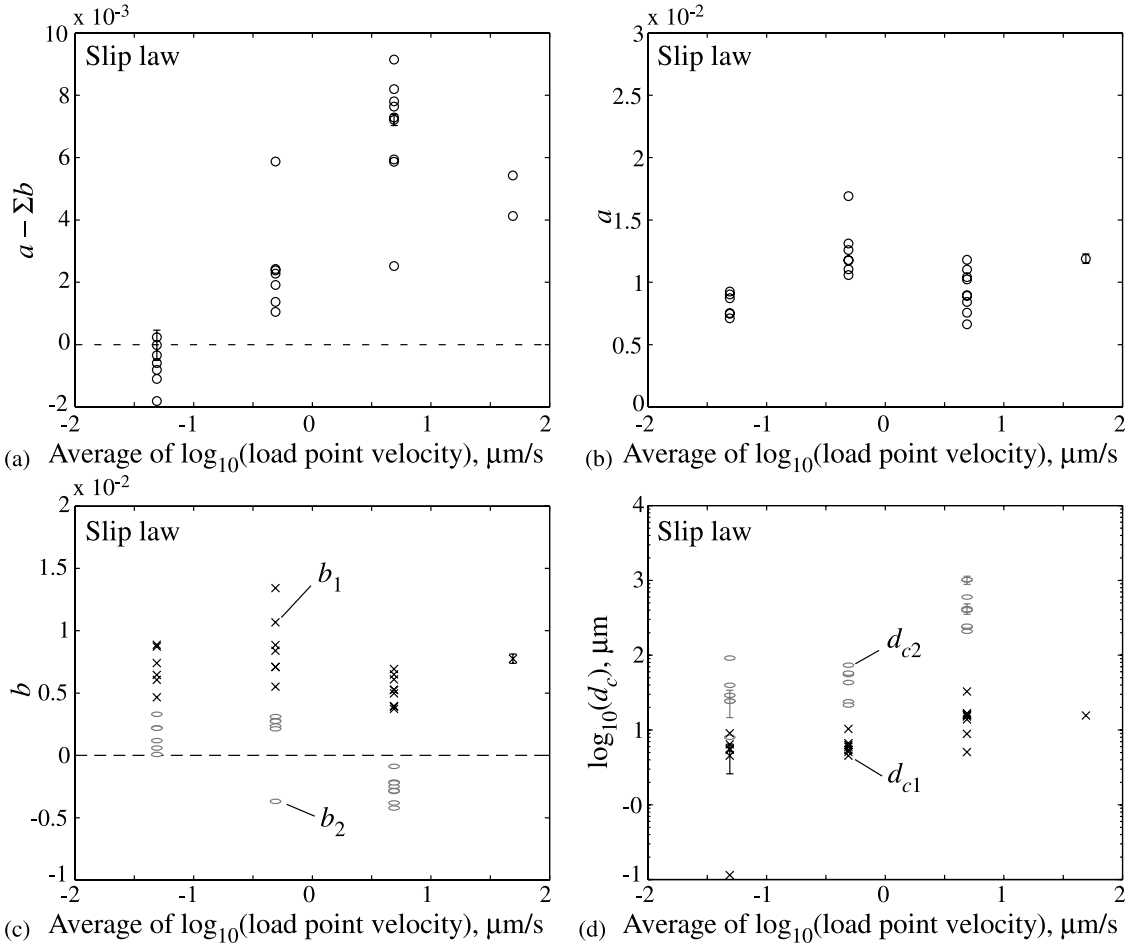

Figure 16. The constitutive parameters determined by numerical least squares fitting with the slip law. The horizontal axes are geometric mean of the slip rates before and after the velocity steps. The error bars ($\pm 2\sigma$) are plotted only when they are longer than the symbol size. If the error is larger than the absolute value of the corresponding optimum parameter value, such a point is not plotted. All results are listed in Table 5. (a) The $a - \Sigma b$ values are determined for all velocity steps. The $a - \Sigma b$ value is negative at a low slip rate and becomes positive at higher slip rates. (b) The a value seems independent of the slip rate. (c) The b values. The b_1 and b_2 are defined so that $d_{c1} < d_{c2}$. If the experimental data are fit well by only one state variable, b is treated as b_1. Typically, at a higher slip rate, a negative b_2 is required to fit the mechanical behavior of the fault. (d) The d_c values. The d_{c2} value increases with slip rate when negative b_2 appears above 1 μm s^{-1}.

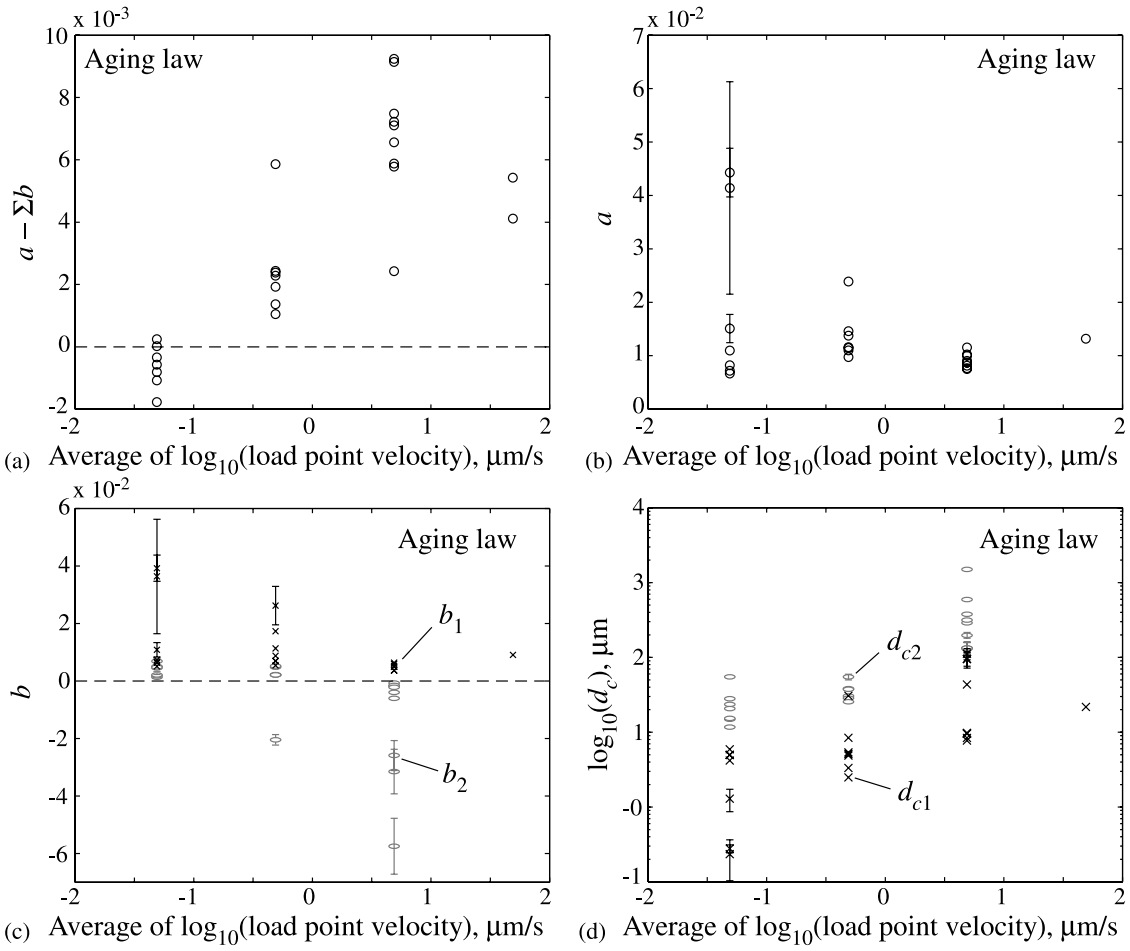

Figure 17. The constitutive parameters determined by numerical least squares fitting with the aging law. The horizontal axes are geometric mean of the slip rates before and after the velocity steps. The error bars ($\pm 2\sigma$) are plotted only when they are longer than the symbol size. If the error is larger than the absolute value of the corresponding optimum parameter value, such a point is not plotted. The overall tendency is not remarkably different from the result with the slip law, but the data points are scattered more widely. All results are listed in Table 6. (a) The $a - \Sigma b$ values. (b) The a values. (c) The b values. (d) The d_c values. The d_{c2} increases with slip rate when negative b_2 appears above 1 μm s^{-1}.

[*Segall and Rice*, 1995]. *Marone et al.* [1990] experimentally observe the increase in the porosity on positive velocity steps for a slip displacement similar to d_c. Then, on a positive velocity step pore pressure might decrease owing to dilatation for the shorter d_{c1} with positive b_1, and increase gradually owing to following fluid transport. This is in the opposite sense to the observed effect of negative b_2.

[60] Figure 19 also imply that the evolution of the second state variable might not be completed before the next velocity step. This is an inherent problem associated with the experimental configuration; the total displacement is restricted. Note that if we waited for a longer strain, $a - \Sigma b$ value might increase owing to the upward convexity for the positive velocity steps although its signature would not change. More experimental works with ring shear apparatus may be needed to fully observe the evolution of second state variable.

[61] In this study, we interpret that at least some of the constitutive parameters vary with the slip rate. Such a treatment makes sense if we formulate the constitutive

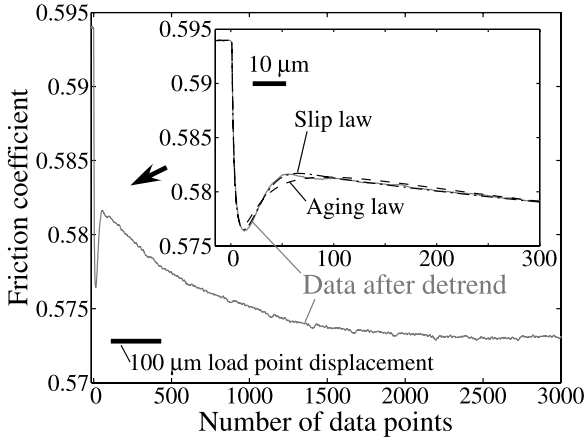

Figure 18. An example (BAF046-13) of the velocity steps which requires negative b_2 after the removal of the trend. The best fit curves are plotted as well in the inset.

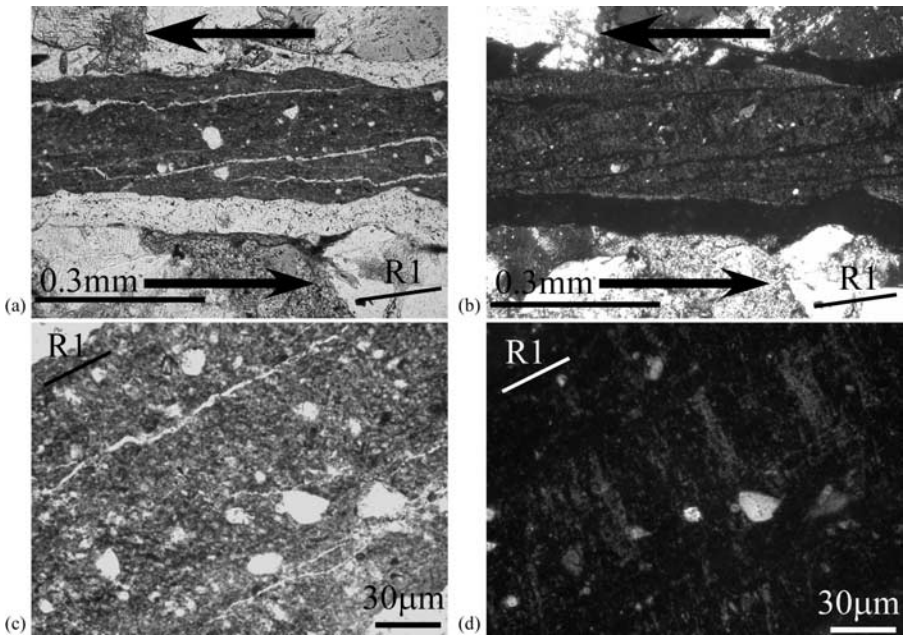

Figure 19. Microphotograph of a sample after an experiment under (a and c) plane-polarized and (b and d) cross-polarized light. R1 planes are often observed which is typically detached because of air drying after the experiment. Y planes are rarely observed. Preferred orientation of platy minerals are observed by forming bands of alternating extinction position (lower) which are cut by R1 planes.

law in a derivative form, equation (1), rather than a standard integrated formulation, $f = f_0 + a \ln(V/V_0) + b \ln(V_0\theta/d_c)$ which might produce a direct effect on V by the third term. The increase in d_c with increasing V has been reported by previous work (e.g., *Logan and Rauenzahn* [1987] for the mixture of quartz and montmorillonite and *Mair and Marone* [1999] for quartz gouge). The conventional interpretation of d_c is that it probably represents the displacement needed to refresh the asperities [*Dieterich*, 1979]. *Marone and Kilgore* [1993] showed that d_c is scaled by the thickness of the shear zone. It should be emphasized that from the point of view of dimensional analysis, the dependency of observed d_c on V has a different meaning from these scaling laws by lengths since it requires a time scale characteristic of the physical process which is responsible to the state evolution. For example, if the state evolution were fully time-dependent process, then an evolution equation might be written as

$$\dot{\theta} = \frac{1}{t_c}(\theta_{ss} - \theta), \tag{22}$$

where t_c is the time scale of the state evolution. This scenario predicts that d_c is proportional to V; $d_c = Vt_c$. This is an extreme example, and our experimental data (Figures 16d and 17d) show much weaker dependency of d_{c1} on V in Figure 17d. How V affects d_c is an interesting future work to investigate the physical process responsible for the state evolution.

[62] Apparently, d_{c2} increases with increasing the slip rate abruptly when b_2 value becomes negative. A possible scenario is that at the low slip rates tested, we need 2 state variables because of the defect in our current formulation of the fault constitutive law, and a new mechanism is activated at around 1 μm s^{-1} which causes the second decay in the opposite direction to usual one (e.g., Figures 17 and 20). A similar behavior is also observed for a sample taken from the detachment at Nankai Trough by ODP Leg 190 [*Kitajima et al.*, 2007]. The transient behavior which requires negative b_2 has been reported by *Weeks and Tullis* [1985] for dolomite, *Marone and Cox* [1994] for gabbro, and *Blanpied et al.* [1998] for granite at high temperature

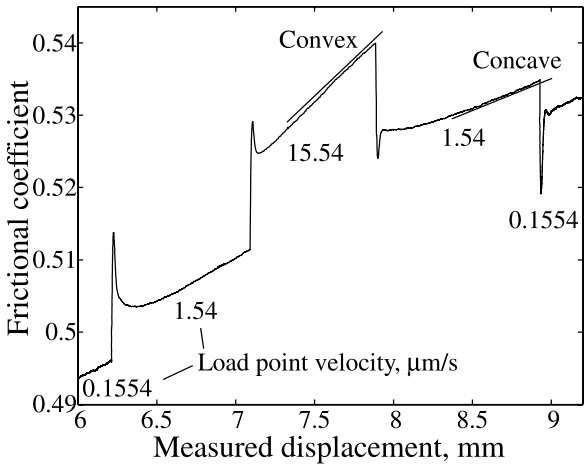

Figure 20. An example of mechanical behavior at relatively high slip rates (BAF046-5, -6, and -7, indicated in Figure 6a). The rate of displacement hardening is apparently higher with upward convexity at 15.54 μm s^{-1}. In the following velocity step, the peak on the velocity step is followed by two decays in positive and negative directions. This behavior is fit by using negative b_2 and long d_{c2} like in Figure 18.

under a hydrothermal condition. The physical process for this effect is unclear, and may be different for rocks. More experimental and observational studies are needed to understand the physical processes which dominantly affect the frictional constitutive behavior of the natural fault.

8. Conclusions

[63] Our detailed investigation of the biaxial friction apparatus in Kyoto University (now moved to Hiroshima University) showed that the machine stiffness has an uncertainty which is shown to be nonnegligible in determining the fault constitutive parameters. This effect is important when the normalized state evolution distance, $\delta_c = d_c/(a/k)$ is not much larger than unity. We thus adopted a method in which the machine stiffness is treated as one of the fitting parameters. Our numerical experiments show that the fault constitutive parameters are successfully recovered with this method.

[64] Frictional experiments on simulated fault with submillimeter thick black clayey fault gouge of the Hanaore Fault (smectite, mica, and quartz) are conducted. The friction coefficient ranges from 0.43 to 0.62 with progressing displacement hardening. The $a - \Sigma b$ value changes from negative to positive around slip rate of 0.1 μm s^{-1}. The overall behaviors of friction coefficient and $a - \Sigma b$ agree with the previous work by *Saffer and Marone* [2003] for mixture of smectite and quartz.

[65] A behavior with 2 state variables (positive b_1 with short d_{c1} and negative b_2 with long d_{c2}) is typically observed at the velocity steps between 1.54 and 15.54 μm s^{-1}. The constitutive parameters are determined by numerical least squares fittings with the stiffness of the apparatus as one of the fitting parameters. Typically, 2 state variables are required to explain the experimental behavior. The a value is around 0.01, and not remarkably dependent on the slip rate. The b_1 does not vary significantly, neither, but b_2 apparently decreases and becomes negative at around 1 μm s^{-1} with increasing slip rate. The d_{c2} increases with slip rate when the negative b value appears. Note that it is always the case that $b_1 > b_2$ and $d_{c1} < d_{c2}$.

[66] Optical microscope observations of samples after the experiments shows a composite plane structure of R1 and bands of alternation of extinction position at high angle from R1. The poor development of Y planes may be consistent with the previous study since the peak strength at the initial yielding is not clear [*Logan et al.*, 1992]. Our low slip rate experiments do not reproduce naturally observed microstructures.

[67] **Acknowledgments.** We appreciate the comments by C. Marone and N. Beeler which improved the manuscript by far. We thank T. Mitchell for checking the grammar and phrasing before submitting the final version. This work is supported by JSPS research fellowship DC1, 17.2149.

References

Andrews, D. J. (2002), A fault constitutive relation accounting for thermal pressurization of pore fluid, *J. Geophys. Res.*, *107*(B12), 2363, doi:10.1029/2002JB001942.

Bizzarri, A., and M. Cocco (2006a), A thermal pressurization model for the spontaneous dynamic rupture propagation on a three-dimensional fault: 1. Methodological approach, *J. Geophys. Res.*, *111*, B05303, doi:10.1029/2005JB003862.

Bizzarri, A., and M. Cocco (2006b), A thermal pressurization model for the spontaneous dynamic rupture propagation on a three-dimensional fault: 2. Traction evolution and dynamic parameters, *J. Geophys. Res.*, *111*, B05304, doi:10.1029/2005JB003864.

Blanpied, M. L., C. J. Marone, D. A. Lockner, J. D. Byerlee, and D. P. King (1998), Quantitative measure of the variation in fault rheology due to fluid-rock interactions, *J. Geophys. Res.*, *103*(B5), 9691–9712, doi:10.1029/98JB00162.

Bos, B., and C. J. Spiers (2002), Fluid-assisted healing processes in gouge-bearing faults: Insights from experiments on a rock analogue system, *Pure Appl. Geophys.*, *159*, 2537–2566, doi:10.1007/s00024-002-8747-2.

Bos, B., C. J. Peach, and C. J. Spiers (2000), Frictional-viscous flow of simulated fault gouge caused by the combined effects of phyllosilicates and pressure solution, *Tectonophysics*, *327*, 173–194, doi:10.1016/S0040-1951(00)00168-2.

Chester, F. M. (1994), Effects of temperature on friction: Constitutive equations and experiments with quartz gouge, *J. Geophys. Res.*, *99*(B4), 7247–7261, doi:10.1029/93JB03110.

Chester, F. M., M. Friedman, and J. M. Logan (1985), Foliated cataclasites, *Tectonophysics*, *111*, 139–146, doi:10.1016/0040-1951(85)90071-X.

Chester, J. S., A. K. Kronenberg, F. M. Chester, and R. N. Guillemette (2003), Characterization of natural slip surfaces relevant to earthquake mechanics, *Eos Trans. AGU*, *84*(46), Fall Meet. Suppl., Abstract S42C-0185.

Dieterich, J. H. (1979), Modeling of rock friction: 1. Experimental results and constitutive equations, *J. Geophys. Res.*, *84*(B5), 2161–2168, doi:10.1029/JB084iB05p02161.

Dieterich, J. H. (1981), Constitutive properties of faults with simulated gouge, in *Mechanical Behavior of Crustal Rocks*, *Geophys. Monogr. Ser.*, vol. 24, edited by N. L. Carter, J. M. Logan, and D. W. Stearns, pp. 103–120, AGU, Washington, D. C.

Di Toro, G., D. L. Goldsby, and T. E. Tullis (2004), Friction falls toward zero in quartz rock as slip velocity approaches seismic rates, *Nature*, *427*, 436–439, doi:10.1038/nature02249.

Di Toro, G., T. Hirose, S. Nielsen, G. Pennacchioni, and T. Shimamoto (2006), Natural and experimental evidence of melt lubrication of faults during earthquakes, *Science*, *311*, 647–649, doi:10.1126/science.1121012.

Fehlberg, E. (1969), Low-order classical Runge-Kutta formulas with step-size control and their application to some heat transfer problems, *NASA Tech. Rep.*, *315*.

Han, R., T. Shimamoto, T. Hirose, J. H. Ree, and J. Ando (2007), Ultra-low friction of carbonate faults caused by thermal decomposition during seismic slip, *Science*, *316*, 878–881, doi:10.1126/science.1139763.

Hirose, T., and M. Bystricky (2007), Extreme dynamic weakening of faults during dehydration by coseismic shear heating, *Geophys. Res. Lett.*, *34*, L14311, doi:10.1029/2007GL030049.

Hirose, T., and T. Shimamoto (2005), Growth of molten zone as a mechanism of slip weakening of simulated faults in gabbro during frictional melting, *J. Geophys. Res.*, *110*, B05202, doi:10.1029/2004JB003207.

Hori, T., N. Kato, K. Hirahara, T. Baba, and Y. Kaneda (2004), A numerical simulation of earthquake cycles along the Nankai trough, southwest Japan: Lateral variation in frictional property due to the slab geometry controls the nuclear ion position, *Earth Planet. Sci. Lett.*, *228*, 215–226, doi:10.1016/j.epsl.2004.09.033.

Hoskins, E. R., J. C. Jaeger, and K. J. Rosengren (1968), A medium-scale direct friction experiment, *Int. J. Rock Mech. Min. Sci.*, *5*, 143–154, doi:10.1016/0148-9062(68)90030-2.

Kawamoto, E., and T. Shimamoto (1997), Mechanical behavior of halite and calcite shear zones from brittle to fully plastic deformation and a revised fault model, in *Proceedings of the 30th International Geological Congress: Beijing, China, 4–14 August 1996*, vol. 14, *Structural Geology and Geomechanics*, edited by Y. Zheng, G. A. Davis, and A. Yin, pp. 89–105, VSP, Utrecht, Netherlands.

Kawamoto, E., and T. Shimamoto (1998), The strength profile for bimineralic shear zones: An insight from high-temperature shearing experiments on calcite-halite mixtures, *Tectonophysics*, *295*, 1–14, doi:10.1016/S0040-1951(98)00112-7.

Kitajima, H., H. Noda, F. M. Chester, and T. Shimamoto (2007), Hydraulic and frictional properties of natural clay-rich sediments from ODP Leg190 Nankai Trough and IODP Expedition 311 Cascadia Margin, *Eos Trans. AGU*, *88*(52), Fall Meet. Suppl., Abstract S21B-0569.

Lachenbruch, A. H. (1980), Frictional heating, fluid pressure, and the resistance to fault motion, *J. Geophys. Res.*, *85*(B11), 6097–6122, doi:10.1029/JB085iB11p06097.

Lapusta, N., and J. R. Rice (2003), Nucleation and early seismic propagation of small and large events in a crustal earthquake model, *J. Geophys. Res.*, *108*(B4), 2205, doi:10.1029/2001JB000793.

Lapusta, N., J. R. Rice, Y. Ben-Zion, and G. Zheng (2000), Elastodynamic analysis for slow tectonic loading with spontaneous rupture episodes on faults with rate- and state-dependent friction, *J. Geophys. Res.*, *105*(B10), 23,765–23,789, doi:10.1029/2000JB900250.

Logan, J. M., and K. A. Rauenzahn (1987), Frictional dependence of gouge mixtures of quartz and montmorillonite on velocity, composition and fabric, *Tectonophysics*, *144*, 87–108, doi:10.1016/0040-1951(87)90010-2.

Logan, J. M., C. A. Dengo, N. G. Higgs, and Z. Z. Wang (1992), Fabrics of experimental fault zones: Their development and relationship to mechanical behavior, in *Fault Mechanism and Transport Properties of Rocks*, edited by B. Evans and T.-F. Wong, pp. 33–67, Academic, London.

Mair, K., and C. Marone (1999), Friction of simulated fault gouge for a wide range of velocities and normal stresses, *J. Geophys. Res.*, *104*(B12), 28,899–28,914, doi:10.1029/1999JB900279.

Marone, C. (1998), The effect of loading rate on static friction and the rate of fault healing during the earthquake cycle, *Nature*, *391*, 69–72, doi:10.1038/34157.

Marone, C., and B. Kilgore (1993), Scaling of the critical slip distance for seismic faulting with shear strain in fault zones, *Nature*, *362*, 618–621, doi:10.1038/362618a0.

Marone, C., C. B. Raleigh, and C. H. Scholz (1990), Frictional behavior and constitutive modeling of simulated fault gouge, *J. Geophys. Res.*, *95*(B5), 7007–7025, doi:10.1029/JB095iB05p07007.

Marone, V., and S. J. Cox (1994), Scaling of rock friction constitutive parameters: The effect of surface roughness and cumulative offset on friction of gabbro, *Pure Appl. Geophys.*, *143*, 359–385, doi:10.1007/BF00874335.

Mase, C. W., and L. Smith (1985), Pore-fluid pressures and frictional heating on a fault surface, *Pure Appl. Geophys.*, *122*, 583–607, doi:10.1007/BF00874618.

Mase, C. W., and L. Smith (1987), Effects of frictional heating on the thermal, hydrologic, and mechanical response of a fault, *J. Geophys. Res.*, *92*(B7), 6249–6272, doi:10.1029/JB092iB07p06249.

Mizoguchi, K., and T. Shimamoto (2004), Dramatic slip weakening of Nojima fault gouge at high-velocities and its implication for dynamic fault motion, *Eos Trans. AGU*, *85*(47), Fall Meet. Suppl., Abstract T23A-0559.

Mizoguchi, K., T. Hirose, T. Shimamoto, and E. Fukuyama (2007), Reconstruction of faulting by high-velocity friction experiments: An example of the 1995 Kobe earthquake, *Geophys. Res. Lett.*, *34*, L01308, doi:10.1029/2006GL027931.

Morrow, C. A., D. E. Moore, and D. A. Lockner (2000), The effect of mineral bond strength and absorbed water on fault gouge frictional strength, *Geophys. Res. Lett.*, *27*(6), 815–818, doi:10.1029/1999GL008401.

Nakae, S., and T. Yoshioka (1998), Geology of Kumakawa district, with geological sheet map at 1:50,000 (in Japanese with English abstract), 71 pp., Geol. Surv. Jpn., Tsukuba.

Nakatani, M. (2001), Conceptual and physical clarification of rate- and state-dependent friction law: Frictional sliding as a thermally activated rheology, *J. Geophys. Res.*, *106*, 13,347–13,380, doi:10.1029/2000JB900453.

Nielsen, H. B. (1999), Damping parameter in Marquardt's method, *Rep. IMM-REP-1999-05*, 31 pp., Dep. of Math. Model., Technical Univ. of Denmark, Lyngby.

Nielsen, S., G. Di Toro, T. Hirose, and T. Shimamoto (2008), Frictional melt and seismic slip, *J. Geophys. Res.*, *113*, B01308, doi:10.1029/2007JB005122.

Niemeijer, A. R., and C. J. Spiers (2006), Velocity dependence of strength and healing behavior in simulated phyllosilicate-bearing fault gouge, *Tectonophysics*, *427*, 231–253, doi:10.1016/j.tecto.2006.03.048.

Noda, H. (2008), Frictional constitutive law at intermediate slip rates accounting for flash heating and thermally activated slip process, *J. Geophys. Res.*, *113*, B09302, doi:10.1029/2007JB005406.

Noda, H., and T. Shimamoto (2005), Thermal pressurization and slip-weakening distance of a fault: An example of Hanaore Fault, southwest Japan, *Bull. Seismol. Soc. Am.*, *95*, 1224–1233, doi:10.1785/0120040089.

Ohnaka, M. (1973), Experimental studies of stick-slip and their application to the earthquake source mechanism, *J. Phys. Earth*, *21*, 285–303.

Reinen, L. A., and J. D. Weeks (1993), Determination of rock friction constitutive parameters using an iterative least square inversion method, *J. Geophys. Res.*, *98*(B9), 15,937–15,950, doi:10.1029/93JB00780.

Reinen, L. A., T. E. Tullis, and J. D. Weeks (1992), Two mechanism model for frictional sliding of serpentinite, *Geophys. Res. Lett.*, *19*(15), 1535–1538, doi:10.1029/92GL01388.

Reinen, L. A., J. D. Weeks, and T. E. Tullis (1994), The frictional behavior of lizerdite and antigorite serpentinies: Experiments, constitutive models, and implications for natural faults, *Pure Appl. Geophys.*, *143*, 317–358, doi:10.1007/BF00874334.

Research Group for Active Faults of Japan (1992), *Maps of Active Faults in Japan With an Explanatory Text*, Univ. of Tokyo Press, Tokyo.

Rice, J. R. (2006), Heating and weakening of faults during earthquake slip, *J. Geophys. Res.*, *111*, B05311, doi:10.1029/2005JB004006.

Rice, J. R., N. Lapusta, and K. Ranjith (2001), Rate and state dependent friction and the stability of sliding between elastically deformable solids, *J. Mech. Phys. Solids*, *49*, 1865–1898.

Ruina, A. L. (1983), Slip instability and state variable friction laws, *J. Geophys. Res.*, *88*(B12), 10,359–10,370, doi:10.1029/JB088iB12p10359.

Saffer, D. M., and C. Marone (2003), Comparison of smectite- and illite-rich gouge frictional properties: Application to the updip limit of the seismogenic zone along subduction megathrusts, *Earth Planet. Sci. Lett.*, *215*, 219–235, doi:10.1016/S0012-821X(03)00424-2.

Segall, P., and J. R. Rice (1995), Dilatancy, compaction, and slip instability of a fluid-infiltrated fault, *J. Geophys. Res.*, *100*(B11), 22,155–22,171, doi:10.1029/95JB02403.

Shibazaki, B., N. Shigematsu, and H. Tanaka (2004), Modeling slip and nucleation processes at the deeper part of the seismogenic zone, *Earth Planets Space*, *56*, 1087–1093.

Shimamoto, T. (1986), Transition between frictional slip and ductile flow for halite shear zones at room temperature, *Science*, *231*, 711–714, doi:10.1126/science.231.4739.711.

Shimamoto, T., J. W. Handin, and J. M. Logan (1980), Specimen-apparatus interaction during stick-slip in a triaxial compression machine: A decoupled two-degree-of-freedom model, *Tectonophysics*, *67*, 175–205, doi:10.1016/0040-1951(80)90234-6.

Shimamoto, T., A. Tsutsumi, T. Hirose, Y. Aizawa, H. Sone, S. Uehara, W. Tanikawa, H. Noda, and K. Mizoguchi (2006), Friction, deformation and fluid-flow apparatus at Kyoto Univ. (in Japanese with English abstract), *Jpn. J. Struct. Geol.*, *49*, 49–71.

Sibson, R. H. (1973), Interaction between temperature and pore-fluid pressure during earthquake faulting—A mechanism for partial or total stress relief, *Nature*, *243*, 66–68.

Sirono, S., K. Satomi, and S. Watanabe (2006), Numerical simulations of frictional melting: Small dependence of shear stress drop on viscosity parameters, *J. Geophys. Res.*, *111*, B06309, doi:10.1029/2005JB003858.

Togo, M., H. Sato, T. Shimamoto, A. Tsutsumi, S. Ma, and T. Nakamura (1997), On the latest paleoseismic event of the Hanaori fault near Kyoto, central Japan (in Japanese with English abstract), *Active Fault Res.*, *16*, 44–52.

Tse, S. T., and J. R. Rice (1986), Crustal earthquake instability in relation to the depth variation of frictional slip properties, *J. Geophys. Res.*, *91*(B9), 9452–9472, doi:10.1029/JB091iB09p09452.

Tsutsumi, A., and T. Shimamoto (1997), High velocity frictional properties of gabbro, *Geophys. Res. Lett.*, *24*(6), 699–702, doi:10.1029/97GL00503.

Tullis, T. E., and D. L. Goldsby (2003), Laboratory experiments on fault shear resistance relevant to coseismic earthquake slip, SCEC Annual Progress Report 2003, South. Calif. Earthquake Cent., Los Angeles.

Tullis, T. E., and J. D. Weeks (1986), Constitutive behavior and stability of frictional sliding of granite, *Pure Appl. Geophys.*, *124*, 383–414, doi:10.1007/BF00877209.

Weeks, J. D., and T. E. Tullis (1985), Frictional sliding of dolomite: A variation in constitutive behavior, *J. Geophys. Res.*, *90*(B9), 7821–7826, doi:10.1029/JB090iB09p07821.

Wibberley, C. A. J., and T. Shimamoto (2005), Earthquake slip weakening and asperities explained by thermal pressurization, *Nature*, *436*, 689–692, doi:10.1038/nature03901.

Yoshioka, T., Y. Kariya, F. Nanayama, A. Okada, and K. Takemura (1998), Latest faulting of the Hanaore fault, central Japan, revealed by trenching studies, and the 1662 Kambun earthquake (in Japanese with English abstract), *J. Seismol. Soc. Jpn.*, *51*, 83–97.

Yoshioka, T., A. Cho, K. Kimura, and S. Nakae (2000), Explanatory text of the strip map of the Hanaore fault, central Japan (in Japanese with English abstract), *Tectonic Map Ser. 13*, scale 1:25,000, 35 pp., Geol. Surv. Jpn., Tsukuba.

H. Noda, Seismological Laboratory, California Institute of Technology, 1200 E. California Boulevard, Mail Code MS 252-21, Pasadena, CA 91125, USA. (hnoda@caltech.edu)

T. Shimamoto, Department of Earth and Planetary Systems Science, Graduate School of Science, Hiroshima University, Higashi-Hiroshima 739-8526, Japan.